AWARD NUMBER: W81XWH-12-1-0284

TITLE: Development of Targeted Nanobubbles for Ultrasound Imaging and Ablation of Metastatic Prostate Cancer Lesions

PRINCIPAL INVESTIGATOR: Mohamed E. El-Sayed

CONTRACTING ORGANIZATION: University of Michigan
Ann Arbor, MI 48109-1274

REPORT DATE: October 2015

TYPE OF REPORT: Final

PREPARED FOR: U.S. Army Medical Research and Materiel Command
                Fort Detrick, Maryland 21702-5012

DISTRIBUTION STATEMENT: Approved for Public Release;
                        Distribution Unlimited

The views, opinions and/or findings contained in this report are those of the author(s) and should not be construed as an official Department of the Army position, policy or decision unless so designated by other documentation.

REPORT DOCUMENTATION PAGE

Form Approved
OMB No. 0704-0188

Public reporting burden for this collection of information is estimated to average 1 hour per response, including the time for reviewing instructions, searching existing data sources, gathering and maintaining the data needed, and completing and reviewing this collection of information. Send comments regarding this burden estimate or any other aspect of this collection of information, including suggestions for reducing this burden to Department of Defense, Washington Headquarters Services, Directorate for Information Operations and Reports (0704-0188), 1215 Jefferson Davis Highway, Suite 1204, Arlington, VA 22202-4302. Respondents should be aware that notwithstanding any other provision of law, no person shall be subject to any penalty for failing to comply with a collection of information if it does not display a currently valid OMB control number. **PLEASE DO NOT RETURN YOUR FORM TO THE ABOVE ADDRESS.**

1. REPORT DATE	2. REPORT TYPE	3. DATES COVERED
October 2015	Final	**15Jul2012 - 14Jul2015**

4. TITLE AND SUBTITLE

Development of Targeted Nanobubbles for Ultrasound Imaging and Ablation of Metastatic Prostate Cancer Lesions

5a. CONTRACT NUMBER

W81XWH-12-1-0284

5b. GRANT NUMBER

5c. PROGRAM ELEMENT NUMBER

6. AUTHOR(S)

Mohamed E.H. ElSayed

E-Mail: melsayed@umich.edu

5d. PROJECT NUMBER

5e. TASK NUMBER

5f. WORK UNIT NUMBER

7. PERFORMING ORGANIZATION NAME(S) AND ADDRESS(ES)

University of Michigan
1101 Beal Avenue
Lurie Biomedical Engineering building
Ann arbor, MI, 48109-2111

8. PERFORMING ORGANIZATION REPORT NUMBER

9. SPONSORING / MONITORING AGENCY NAME(S) AND ADDRESS(ES)

U.S. Army Medical Research and Materiel Command
Fort Detrick, Maryland 21702-5012

10. SPONSOR/MONITOR'S ACRONYM(S)

11. SPONSOR/MONITOR'S REPORT NUMBER(S)

12. DISTRIBUTION / AVAILABILITY STATEMENT

Approved for Public Release; Distribution Unlimited

13. SUPPLEMENTARY NOTES

14. ABSTRACT

In this project, we developed the amphiphilic PEG-*b*-(PAA)-*b*-P(HDFMA-*co*-MMA) copolymers that can encapsulate PFP or PFH forming nanodroplets (~200 nm). Combining these nanodroplets with histotripsy proved to generate a cavitation bubble cloud with similar behavior but lower pressure compared to histotrpsy itself. We investigated physical mechanisms underlying the nanodroplet cavitation process with playing different transducer frequencies (0.345, 0.5, 1, 3 MHz), changing the core PFC (PFP: boiling point 29 $^\circ$C or PFH: boiling point 56 $^\circ$C) and as well as cavitation nucleation is caused by the negative pressure (*p*-) exposed to the PFC. Under the light of these findings we established nanodroplet mediated histotripsy cell cavitation on 3D prostate cancer spheroid models..

15. SUBJECT TERMS

Nanodroplets, mechanical cell fractionation, histotripsy, lower pressure threshold

16. SECURITY CLASSIFICATION OF:			17. LIMITATION OF ABSTRACT	18. NUMBER OF PAGES	19a. NAME OF RESPONSIBLE PERSON USAMRMC
a. REPORT	**b. ABSTRACT**	**c. THIS PAGE**	UU	34	19b. TELEPHONE NUMBER *(include area code)*
U	U	U			

Table of Contents

1. INTRODUCTION

Current tumor ablation methods have limitations like low targetibility, which ma cause killing both cancer and surrounded healthy cells[2] and poor imaging ability as a problem for early stage and micro-metastasis[3]. However, the ideal tumor ablation method would provide noninvasive treatment of cancer cells at all stages without damage to surrounding non-cancerous cells. To overcome this problem different ablation techniques were combined with microbubbles. In this case, microbubbles was too high to penetrate into tumor`s interstitial space. Recently, nanodroplets that can extravasate to a tumor's interstitial space have been developed for targeted imaging[4] and drug delivery,[5] but have yet to be utilized for targeted ablation. To address this point, we started working on combining PFC-encapsulated nanodroplets with histotripsy, which is a new, non-invasive, image-guided, ultrasound ablation method.[6] Histotripsy uses extremely high pressure, microseconds long pulses to generate a cluster of microbubbles (bubble cloud) from pre-existing gas pockets in the tissue where the rapid expansion and collapse of the microbubbles disrupts cells.[6b, c, 6e] We hypothesize that PFC-loaded nanodroplets with an average diameter < 500 nm can diffuse across tumor's leaky vasculature and accumulate in the cancer lesion when administered into the systemic circulation.[7] Applying specific US pulse sequences to the tumor lesion will deliver the acoustic energy necessary to convert the PFC core from the liquid to the gaseous phase which will allow real time US imaging of tumor tissue. Unlike histotripsy that relies on cavitation nuclei derived from rare gas pockets in the tissue and extremely high acoustic pressures to initiate the cavitation process, the gas bubbles formed by ADV can act as cavitation nuclei to generate and maintain the cavitation bubble cloud at a significantly reduced pressure. The significantly reduced cavitation threshold will allow us to deliver histotripsy to the tumor tissue "tagged" with the nanodroplets resulting in selective fractionation of cancer cells while sparing the surrounding normal tissue.

2. BODY

Task 1. Formulation and characterization of targeted nano-bubble contrast agents: *To develop a strategy to formulate nano-bubble contrast agents with tunable size, PFP content, and shell flexibility to obtain stable and echogenic nano-bubbles. In regarding to this task we published two manuscripts, first "Development of nanodroplets for histotripsy-mediated cell ablation", which showed that the synthesis and characterization of the PFP-loaded nanodroplets (See Appendix 1 for original paper). Second one "Nanodroplet-mediated histotripsy for image-guided targeted ultrasound cell ablation" described the ability to combine our nanodroplets with histotripsy to achieve efficient red blood cell (RBC) ablation in tissue-mimicking phantoms (See Appendix 2 for original paper).*

A. _Synthesis and characterization of amphiphilic block copolymer:_ A series of amphiphilic block copolymer was synthesized to be able to formulate nano-bubble contrast agents with tunable size, PFP content, and shell flexibility to obtain stable and echogenic nano-bubbles. The effect of the molar ratio of hydrophilic and hydrophobic monomers and polymer`s molecular weight on the size of nano-bubble were investigated. The results indicated that there are two compositions (ABC-1 and ABC-2 in **Table 1**) better than others in terms of nanodroplets stability and loading capacity. Based on these prescreen we focused on these two compositions in order to optimize conditions for cell ablation. To be able to obtain well-defined amphiphilic block copolymers, individual blocks were prepared separately and combined via one-pot click reaction (**Figure 1**). 2 and 5 KDa PEG with alkyne functionality were prepared through esterification to incorporate into ABC block copolymers and conjugation efficiency was confirm by ^{1}H NMR as > 95 % for both case. Crosslinkable block obtained via atom transfer radical polymerization (ATRP) has a constant length (10 units) for both copolymer compositions in order to eliminate possible effect of shell thickness on phase transition. This length ideally
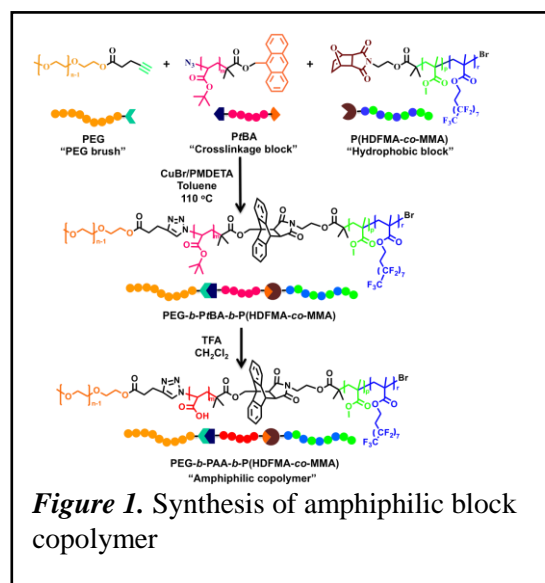

Figure 1. Synthesis of amphiphilic block copolymer

forms a thin cross-linked shell that stabilizes nanodroplets while allowing phase transition. It was initially synthesized as anthracene functional poly(*tert*-butyl acrylate)-Br (Anth-P*t*BA-Br) which not only carries the functionality for DA "click" reaction but also carries bromine group that can be easily transferred into azide group for azide-alkyne click reaction. It is a common strategy to obtain hydrophilic poly(acrylic acid) (PAA) from P*t*BA by simply hydrolysis of *tert*-butyl groups using trifluoroacetic acid (TFA). In order to

| Table 1. Composition of amphiphilic PEG-*b*-PAA-*b*-P(HDFMA-*co*-MMA) copolymers.								
Polymer	$M_{n,PEG}$ (g/mol) (# of units)	$M_{n,PtBA}$[a,b] (g/mol) (# of units)	$M_{n,P(MMA-co-HDFMA)}$[a] (g/mol) (# of units)	$M_{nHP}/$ M_{nHF}[c]	# of HP/# of HF units[d]	$M_{n,ABC}$[a] (g/mol)	$M_{n,ABC}$[e] (g/mol)	PD[e]
ABC-1	2000 (45)	1640 (10)	6720 (29)	1.84	**0.53**	10370	9613	1.11
ABC-2	5000 (113)	1640 (10)	11390 (52.5)	1.71	**0.42**	18040	17510	1.12

[a] Calculated from ^{1}H NMR spectra. [b] *Tert*-butyl groups were efficiently hydrolyzed into acid group to obtain the final ABC block copolymer. [c] M_{nHP}/M_{nHF}: Molecular weight of hydrophobic block (HP)/molecular weight of hydrophilic blocks (HF). [d] # of HP/# of HF units: The number of hydrophobic units (HP)/the number of hydrophilic units. [e] Determined by gel permeation chromatography (GPC) using Styragel HR 4E column compared to a series of PMMA standards (PolyAnalitik Inc, Canada) using THF as a mobile phase at a flow rate of 1 ml/min at 35 °C. Data were analyzed using Viscotek OmniSEC Omni-

investigate the effect of the number of fluorinated monomer units and molecular weight of fluorinated block on loading capacity, P(HDFMA-*co*-MMA) copolymers were designed with two different molecular weight and the number of HDFMA units. Since, most of the fluorinated monomer`s homopolymer has a solubility problem[8], MMA was used as a co-monomer to solubilize HDFMA containing copolymer and copolymerized with HDFMA to obtain fluorinated hydrophobic block with two different degree of polymerization via ATRP using DA reactive protected maleimide functional initiator (*Figure 1*). Copper catalyzed azide-alkyne cycloaddition (CuCAAC) between The successful coupling was initially confirmed by ^{1}H NMR spectroscopy. Aromatic protons of anthracene (7.4-8.6 ppm) were completely disappeared while new Diels-Alder cycloadduct protons were appeared with triazole ring proton as an indication of successful dual click reactions.

Molecular weight and molecular weight distribution of PEG-*b*-P*t*BA-*b*-P(HDFMA-*co*-MMA) copolymers were also measured using gel permeation chromatography (GPC). Finally,

Figure 2. Self-assembly of amphiphilic copolymer into PFP-loaded nanodroplets.

PEG-*b*-P*t*BA-*b*-P(HDFMA-*co*-MMA) copolymers were hydrolyzed using TFA in order to obtain COOH functionality that can react with diamine functional crosslinker to form a crosslinked shell after self-assembly of block copolymer into nanodroplets. The success of reaction was monitored using ^{1}H NMR which showed complete reduction on methyl protons of *tert*-butyl groups at 1.43 ppm for PEG-*b*-PAA-*b*-P(HDFMA-*co*-MMA) copolymers (ABC-1 and ABC-2) (*Figure 1*).
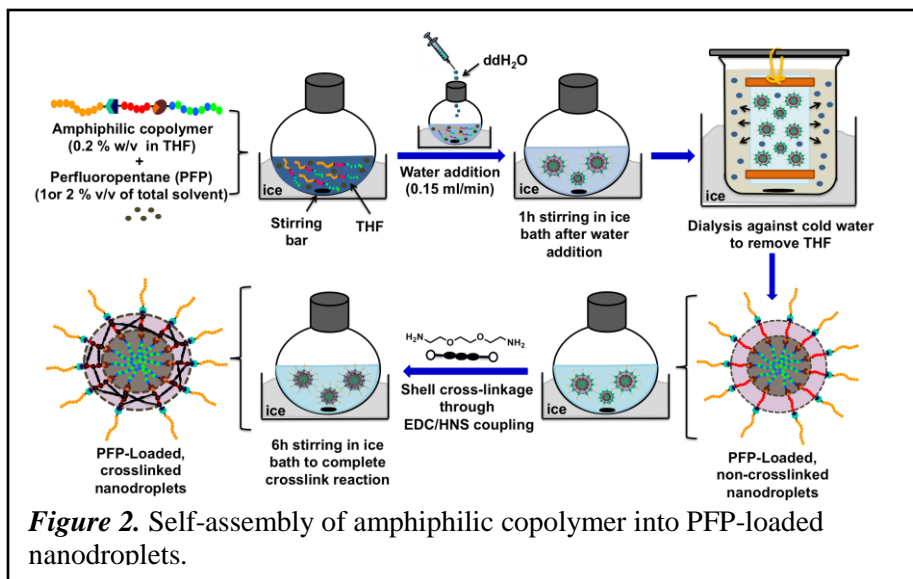
B. Preparation and Chacterization of Shell Cross-linked Nanodroplets: Once we obtained well-defined triblock copolymers (ABC-1 and ABC-2) where the molecular weight of the P(HDFMA-*co*-MMA) (6.5kDa and 11.5kDa) and PEG (2kDa and 5kDa), we prepared different amounts of PFP (1% and 2% v/v) nanodroplets to examine their encapsulation efficiency and overall droplets stability. *Figure 2* describes the self-assembly of amphiphilic ABC-1 and ABC-2 polymers around the PFP core with variable PFP content (0%, 1%, and 2% v/v). ABC-1 and ABC-2 copolymers were dissolved in tetrahydrofuran (THF) followed by cooling down the polymer solution in an ice bath and adding different volumes of PFP (0%, 1%, or 2% v/v) while mixing. An equal amount of water was slowly added to the polymer/PFP mixture to initiate polymers self-assembly into nano-sized micelles that will encapsulate the hydrophobic PFP solution forming nanodroplets. This solution mixture was kept stirring on an ice bath for 1 hour before transferring to a dialysis bag and dialyzing against ice cold water for 12 hours to yield a homogenous milky solution indicating nanodroplets formation. We used 2,2`-(ethylenedioxy)-bis(ethylamine) linker to crosslink the polymer chains via standard NHS/EDC coupling reactions with the central PAA units.[9] Cross-linked nanodroplets were further purified by dialysis against ice-cold water before their characterization and subsequent use in ablation studies. We confirmed the cross-linkage

Figure 3. Thermal properties of P(HDFMA-*co*-MMA), PEG-*b*-PAA-*b*-P(HDFMA-*co*-MMA) (ABC-1), non-crosslinked micelles and crosslinked micelles made out of ABC-1 block copolymer.

Table 2. Thermal properties of nanodroplets and its precursors.

Polymer	1st Transition (T_m for PEG) °C[a]	2nd Transition (T_g) °C[a]
P(HDFMA-*co*-MMA)-1	-	61.4
P(HDFMA-*co*-MMA)-2	-	76.5
ABC-1	50.8	60.9
ABC-2	57.2	62.5
NCL-ND-ABC-1[b]	50.9	60.7
CL-ND-ABC-1[b]	47.5	79.1
NCL-ND-ABC-2[b]	55.5	63.9
CL-ND-ABC-2[b]	54.2	65.0

[a] Determined by Differential Scanning Calorimetry (DSC). [b] PFP encapsulated nanodroplets were lypholized before DSC measurement.

of the central PAA block by examining the thermal behavior of the amphiphilic polymer (e.g. ABC-1), the hydrophobic P(HDFMA-*co*-MMA) block, cross-linked droplets, and non-cross-linked droplets when heated
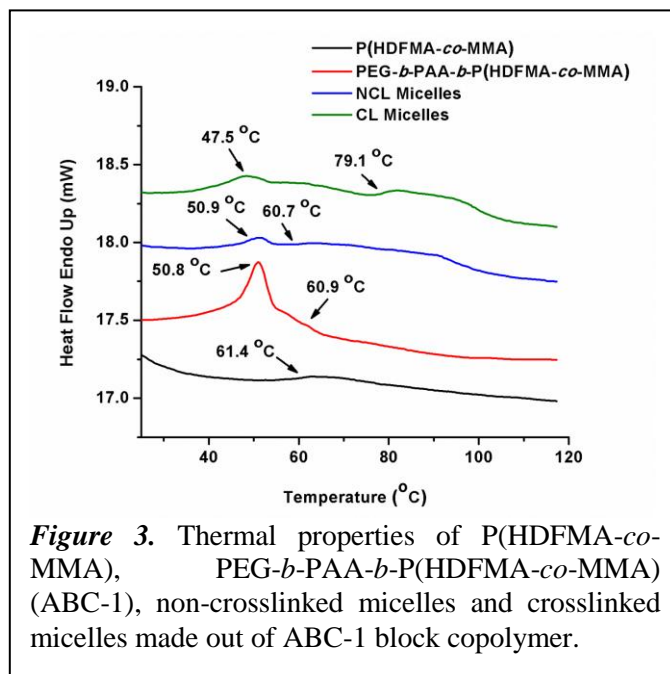
Table 3. Properties of the nanodroplets prepared using ABC-1 and ABC-2 polymers.

| Nanodroplets Code	Mode Size at 22°C (nm)[a]	Concentration at 22°C (10^10 Particles/mL)[a]	Mode Size at 37°C (nm)[a]	Concentration at 37°C (10^10 Particles/mL)[a]	Zeta Potential (mV)[b]
ND-ABC-1-0% PFP	164.5±8.5	2.31±0.08	162.0±6.5	2.96±0.07	0.1±0
ND-ABC-1-1% PFP	117.5±9.7	2.50±0.05	111.9±6.8	2.58±0.04	0.0±0
ND-ABC-1-2% PFP	126.3±8.0	3.07±0.11	135.3±7.1	3.00±0.12	0.0±0
ND-ABC-1-0% PFP	178.9±7.4	2.98±0.10	187.3±10.8	2.98±0.09	0.0±0
ND-ABC-2-1% PFP	163.0±11.1	3.59±0.09	167.0±9.0	4.09±0.11	0.0±0
ND-ABC-2-2% PFP	159.1±6.2	4.41±0.11	166.8±4.3	4.85±0.12	0.0±0

[a] Mode size represents the most abundant fraction in the nanodroplets solution calculated using Nanoparticles Tracking Analysis (NTA) and NTA 2.3 build 127 software. Results are the average of 6 measurements of a minimum of 3 independent experiments ± standard error of the mean (SEM). [b] Measured using 90Plus particle size analyzer with Zeta PALS capability at room temperature.

between 20-120°C using a differential scanning calorimeter. The P(HDFMA-*co*-MMA) block with an

average molecular weight of 6.7 kDa has a glass transition temperature (T_g) of 61.4°C, which increased to 76.5°C with the increase in molecular weight to 11.4 KDa (*Figure 3 & Table 2*). Since the PEG and P(HDFMA-*co*-MMA) blocks are not miscible, the thermograph of ABC-1 polymer shows two transitions at 50.8°C and 60.9°C corresponding to the PEG melting point and T_g of the P(HDFMA-*co*-MMA) block, respectively (*Figure 3*). Increasing the molecular weight of the PEG and P(HDFMA-*co*-MMA) blocks increased their melting point and T_g, respectively (*Table 2*). The restricted mobility of the polymer chains in cross-linked droplets prepared using ABC-1 polymer caused an increase in the T_g compared to the parent polymer and non-cross-linked droplets. However, the insignificant difference in the T_g between cross-linked and non-cross-linked droplets prepared using ABC-2 is due to the increase in PEG content (38%) compared to ABC-1 (24%), which acts as a plasticizer and reduce the observed T_g as shown in previous reports.[10]

We used Nanosight NS500 (NanoSight Limited, Amesbury, United Kingdom) equipped with a sample chamber with a 640nm laser and a fluoroelastomer O-ring to measure the size and concentration (i.e. number of nanodroplets/mL) of cross-linked (CL) nanodroplets formulated using ABC-1 and ABC-2 polymers as a function of PFP loading (0%, 1%, and 2% v/v) at room (22°C) and body (37°C) temperatures.

Figure 4. Size of cross-linked nanodroplets prepared using ABC-1 and ABC-2 polymers with different PFP content (0%, 1%, and 2% v/v) at: (A) 22°C and (B) 37°C calculated using the Nanoparticle Tracking Analysis (NTA) 2.3 software. Results are reported as the average of six different measurements collected from three independent solutions + standard error of the mean

We relied on the Nanoparticle Tracking Analysis (NTA) 2.3 software to capture and analyze images of different nanodroplets solutions and calculate the average size of each formulation (*Figure 4*). Results show that nanodroplets formulated using ABC-1 polymer have average diameter of 192±4.7-218±2.1nm at 22°C, which slightly increased to 201±2.61-211±4.7nm at 37°C (*Figure 4*). Nanodroplets formulated using ABC-2 polymer have average diameter of 202±2.7-236±2.6nm at 22°C, which also slightly increased to 206±2.9-246±3.4nm at 37°C. Results show that the increase in PFP loading from 0%-2% v/v did not influence the average size of all the formulated nanodroplets. It is important to note that NTA software identified the major fraction in each formulation and calculated its average mode size and concentration (*Table 3*). Results show that the average "mode size" for ND-ABC-1-1% and ND-ABC-1-2% droplets at 37°C is 111.9±6.8nm and 135.3±7.1nm, respectively. Similarly, the average mode size for ND-ABC-2-1% and ND-ABC-2-2% droplets at 37°C is 167.0±9.0nm and 166.8±4.3nm, respectively. These results clearly show that the

Figure 5. (A) A schematic drawing of the experimental setup incorporating a 500 kHz transducer attached to a motorized 3D positioning system controlled using a PC console. Formation of a bubble cloud in response to histotripsy treatment was monitored using high-speed optical imaging (Phantom V210, Vision Research). (B) A schematic drawing showing the expansion of the nanodroplets (100-350nm) forming microbubbles (> 500µm) before energetically collapsing and mechanically fractionating neighboring cells.

average size of cross-linked (CL) nanodroplets prepared using ABC-1 and ABC-2 polymers with different PFP content is much smaller than the size cutoff (~500nm) of the tumor vasculature.[11] Furthermore, the concentration of cross-linked ND-ABC-1 and ND-ABC-2 nanodroplets did not decrease upon increasing the solution temperature from 22°C to 37°C, which indicates droplets resistance to dissolution and stability at
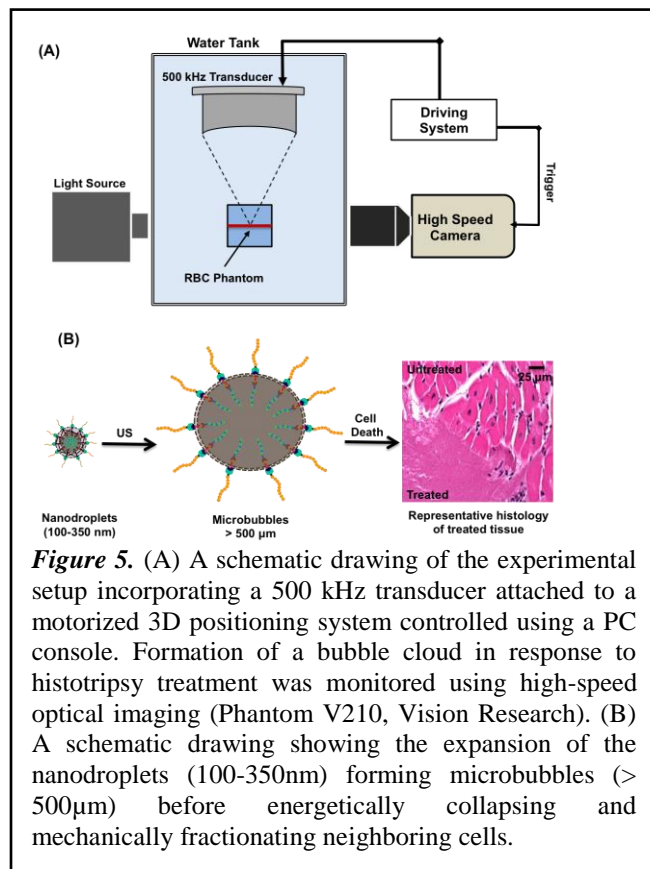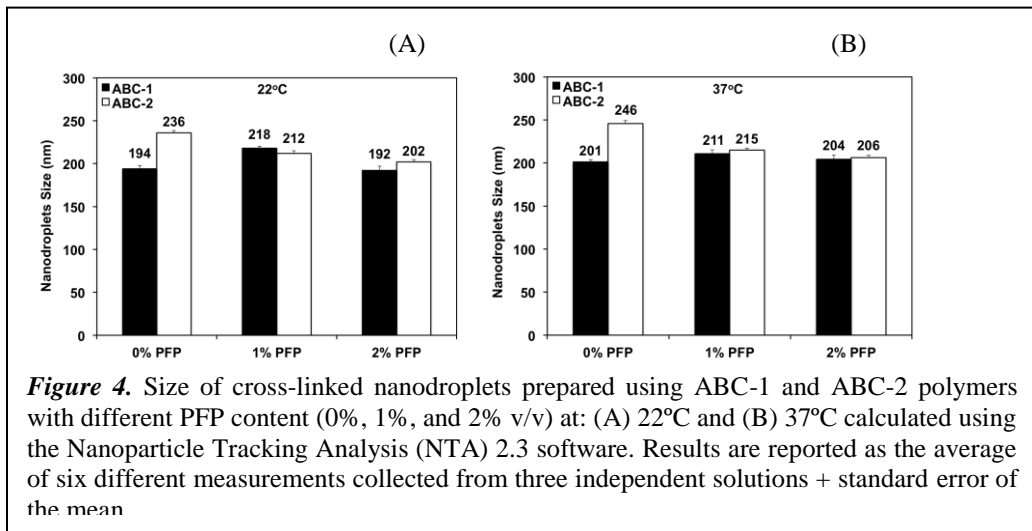
body temperature (***Table 3***). These results collectively indicate the promise of these nanodroplets in future *in vivo* evaluation.

We used 90Plus particle size analyzer with ZetaPALS capability (Brookhaven Instruments Corporation, Holtsville, NY) to measure the zeta potential of nanodroplets formulations, which was ~0 mV indicating a neutral droplets surface (***Table 3***).

C. Measurement of Histotripsy Threshold in Agarose Tissue Phantoms:

Agarose tissue phantoms (1% w/v) have been used as model tissue phantoms to investigate the ablative effects of histotripsy therapy.[12] To compare the effects of our nanodroplet-mediated ablation to histotripsy alone at higher pressure, we treated agarose tissue phantoms (1% w/v) containing each of our nanodroplet formulations (***Figure 5***). Briefly, the agarose phantom was placed in the focal zone of a 32 element, 500 kHz, transducer inside a degassed water tank at $37^{\circ}C$ (***Figure 5, Panel A***). A high-speed, 1 megapixel CCD camera (Phantom V210, Vision Research) was positioned to image the plane of the RBCs layer throughout the histotripsy treatment using a flash lamp as a backlight for the phantom to record the bubble cloud formed from the expansion of the embedded nanodroplets into microbubbles. We hypothesized that ultrasound treatment of the embedded nanodroplets will

Figure 6. A plot showing the histotripsy threshold in agarose tissue phantoms with and without nanodroplets. Results demonstrated a significant decrease in the pressure threshold to generate cavitation bubbles >50 μm with nanodroplets compared to control conditions (histotripsy only).

trigger acoustic droplet vaporization forming microbubbles, which will expand reaching an average size > 50μm before they violently collapse causing disruption of the neighboring RBCs (***Figure 5B***). Disruption of the translucent RBCs layer renders the agarose gel more transparent, which provides visual evidence of cell ablation. Previous work has demonstrated that damage to the RBC tissue phantoms directly correlates to the tissue damage formed by histotripsy therapy.[12] The pressure threshold to vaporize the nanodroplets and expand the resulting bubbles >50 μm was measured in tissue-mimicking agarose phantoms with and without nanodroplets. Based on the analysis of high-speed images, results demonstrated a significant decrease in the histotripsy threshold with nanodroplets compared to histotripsy only controls. The minimum pressure level at which cavitation bubbles >50 μm was observed by high speed images to be 3.02±2.49 MPa for phantoms containing nanodroplets and 15.60±2.35 MPa for histotripsy only controls without nanodroplets (***Figure 6***).

D. Ablation of Red Blood Cell in Tissue Phantom:

Agarose tissue phantoms (1% w/v) with an embedded layer of red blood cells (RBCs) have been used as model tissue phantoms to investigate the ablative effects of histotripsy therapy. We tested our hypothesis by applying histotripsy pulses to the center of the agarose gels at the RBC layer using a pulse repetition frequency of 10Hz at a peak negative pressure of 20.7MPa. We embedded an equal number of nanodroplets (2.36×10^{8} droplets/mL) in the agarose gel to eliminate the effect of droplets concentration on the observed ablation behavior but rather focus on investigating the effect of polymer composition (ABC-1 versus ABC-2) and PFP content (0%, 1%, and 2% v/v) on ablation capacity to identify the most effective formulation. Results show that histotripsy application could not initiate a bubble cloud from empty nanodroplets (i.e. 0% PFP loading)
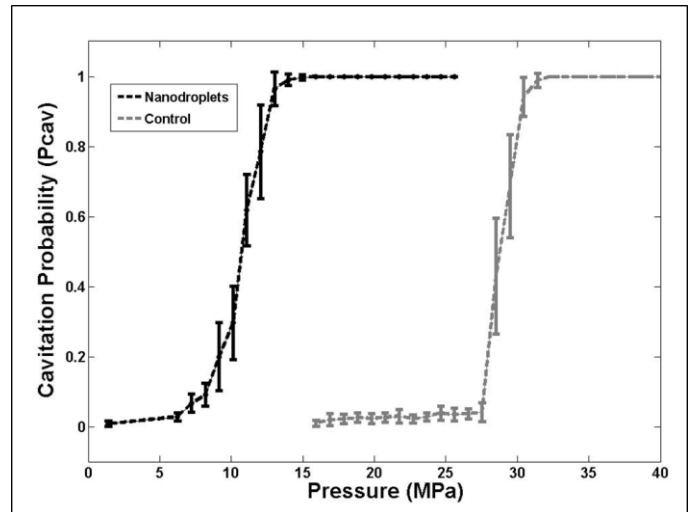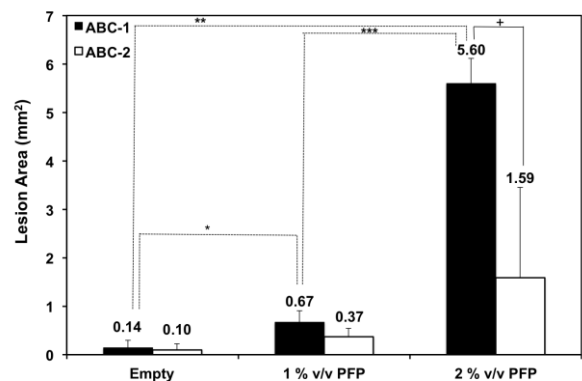

Figure 7. The area of the ablation zone (mm^2) observed after treatment of agarose gels using different nanodroplet formulations calculated using MATLAB (The Math-Works, Natick, MA, USA).

6

prepared using ABC-1 and ABC-2 polymers at the applied acoustic pressure (20.7MPa) and no damage was observed in the RBCs layer. A similar histotripsy application to tissue phantoms containing nanodroplets prepared using ABC-1 polymer loaded with 1% and 2% v/v PFP resulted in the formation of a bubble cloud in the center of the gel and formation of a corresponding transparent zone confirming the ablation of the RBCs. The nanodroplets prepared using ABC-2 polymer and loaded with 1% and 2% v/v PFP also resulted in cavitation and lesion formation in response to the histotripsy treatment.

Figure 8. Optical images of nanodroplet-mediated cell fractionation. Images of cavitation bubble cloud (dark) and lesions (white) generated in the RBC agarose gel (grey) using nanodroplet-mediated histotripsy at different pressure levels. A total of 2000 2-cycle pulses at 10 Hz PRF were used for each treatment.

We measured the surface area of the lesions formed in each tissue phantom and plotted it against nanodroplets composition and PFP content (**Figure 7**). Results show that empty nanodroplets (i.e. 0% PFP loading) caused no ablation to RBCs regardless of the polymer composition used to formulate the nanodroplets. This demonstrates that the loading of PFP in the droplets' core is critical for bubble formation in response to histotripsy treatment. Increasing PFP content from 1% to 2% v/v caused an increase in the surface area of the ablation lesion from $0.67\pm0.23\text{mm}^2$ to $5.60\pm0.52\text{mm}^2$ (8.4 folds) for nanodroplets prepared using ABC-1 polymer. Similarly, increasing PFP content in the nanodroplets prepared using ABC-2 polymer from 1% to 2% v/v increased the surface area of the ablation lesion from $0.37\pm0.17\text{mm}^2$ to $1.59\pm1.86\text{mm}^2$ (4.3 folds). It is interesting to note that nanodroplets prepared using ABC-1 polymer exhibit higher ablation capacity compared to those prepared using ABC-2 polymer, which can be attributed to difference in polymer's capacity to encapsulate and retain the loaded PFP. Specifically, ABC-2 polymer has an average of 13.5 units of the fluorinated monomer with the heptadecafluorodecyl groups distributed along a long hydrophobic backbone, which results in strong interaction of the hydrophobic block in the droplets core that limits PFP loading and encapsulation.

Our results are supported by previously published results showing that the number of fluorinated monomers plays a critical role in PFC loading and encapsulation by a polymeric shell.[13] For example, Yokoyama and coworkers synthesized a series of amphiphilic PEG-*b*-poly(fluoroheptyl aspartate) copolymers with a variable number of fluorinated alkyl chains and investigated their ability to encapsulate PFC forming nanodroplets.[13] Results show that introducing 10% of fluoroheptyl units in the polymer backbone was sufficient to encapsulate the loaded

Figure 9. Selective cavitation in a composite agarose tissue phantom. Optical images (top) of agarose phantoms with hexagon shaped inclusions containing nanodroplets demonstrated cavitation within the focal area only occurred in locations containing nanodroplets while no cavitation was observed in regions without nanodroplets. Ultrasound imaging (bottom) demonstrated nanodroplet guided cavitation treatment can be monitored in real-time with bubbles appearing as dynamically changing hyperechoic regions.

PFP (45.5 mg/mL) forming nanodroplets. Incorporation of higher or lower percentages of fluoroheptyl units in the polymer backbone reduced PFP encapsulation by the polymer and negatively affected droplets stability. Further, the increase in the number of fluorinated carbon atoms in the fluoroalkyl chain above 9
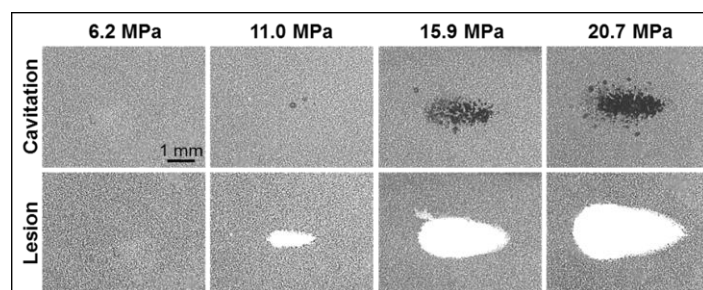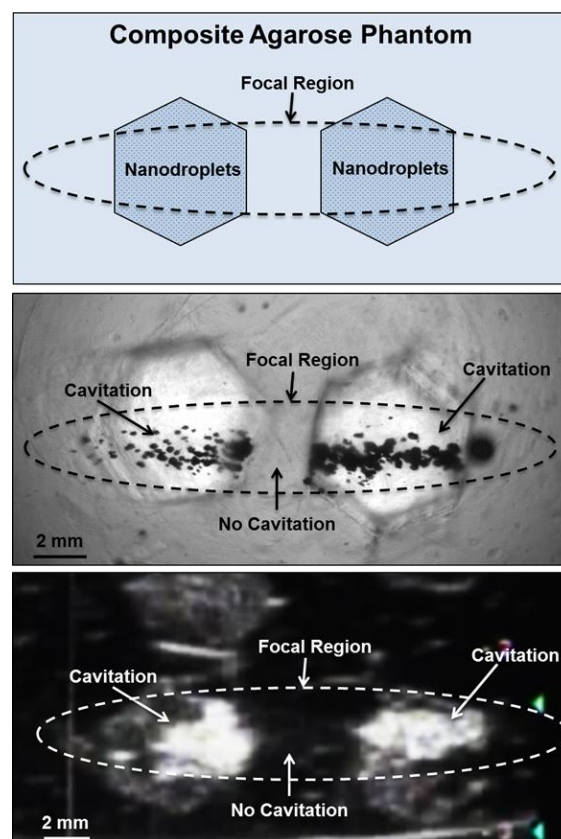
decreases the encapsulation of PFP. These results collectively show that the nanodroplets formulated using ABC-1 polymer and loaded by 2% PFP exhibit the highest ablation capacity among all formulations.

Once we determined the best composition and loaded PFP %, a detail investigation was performed using this composition. At peak negative pressure below 10 MPa, no microbubbles were observed and no lesions were visualized. At peak negative pressure of 11.0 MPa and greater, when cavitation bubbles were generated, well-defined lesions were formed in the RBC phantoms using nanodroplets combined with histotripsy (*Figure 8*). Nanodroplet-mediated histotripsy fractionated the RBC phantom with similar efficiency to histotripsy at higher pressure with all RBCs within the focal volume completely fractionated within 2,000 pulses, resulting in transparent lesions with no intact RBCs remaining. The area of lesion in the RBC layer increased with increasing pressure. For example, the lesion areas for RBC phantoms containing nanodroplets (n=6) were 0.77 ± 0.09 mm^2, 3.92 ± 0.41 mm^2, and 6.27 ± 0.86 mm^2 for peak negative pressures of 11.0 MPa, 15.9 MPa, and 20.7 MPa, respectively (*Figure 8*). In comparison, in control gels without nanodroplets, no lesions were formed at any treatments in this pressure range. These results are important to show that nanodroplet-mediated cavitation can indeed create cell disruption with the same effectiveness (i.e., the same number of pulses) as using histotripsy alone but at a significantly lower pressure. This is an important validation of our hypothesis confirming that the cavitating microbubbles generated via nanodroplets are destructive to use for ablation.

E. Selective Cavitation in Composite Agarose Phantom: Based on the reduced histotripsy threshold using nanodroplets, cavitation should be selectively generated in multi-tumor nodules with nanodroplets inside the focal zone, whereas no cavitation should be formed at normal tissue without nanodroplets. The feasibility of using nanodroplets to generate selective cavitation was investigated using a composite agarose tissue phantom. Histotripsy pulses were applied inside the composite agarose tissue phantom containing inclusions with nanodroplets. Using 2-cycle pulses at a peak negative pressure of 17.3 MPa, which is above the histotripsy threshold using nanodroplets and below the intrinsic threshold using histotripsy alone, cavitation bubble clouds were formed only in the inclusions containing nanodroplets located within the focal volume of the 500 kHz transducer (*Figure 9, top*). Optical images indicated two separate dense cavitation clouds inside the nanodroplet-containing inclusions inside the focal region throughout the 2000 pulses while no bubbles were observed outside the inclusions within the focal region (*Figure 9 middle*). Correspondingly, ultrasound imaging showed two dynamically changing hyperechoic zones inside the hexagon inclusions, while no bubbles were observed elsewhere (*Figure 9, bottom*). As these cavitation bubbles generated in the process are viewed clearly on ultrasound imaging, the histotripsy therapy process can be monitored and guided by ultrasound imaging in real-time.

F. Bubble Behavior: The bubble expansion and collapse observed in histotripsy is substantially more energetic than traditionally defined inertial cavitation where the maximal bubble diameter becomes equal or greater than twice the initial bubble size.[14] In histotripsy, microbubbles formed from preexisting nuclei <10 nm grow to over 50 μm before violently collapsing, all occurring within 100 μs. This bubble behavior is critical to achieve cell disruption. To study the behavior of cavitation bubbles generated by nanodroplet-mediated histotripsy, optical images of bubbles were recorded by the high-speed camera at different time delays after the arrival of the histotripsy pulse. The peak negative pressure of 15.6 MPa was used, because it is the lowest pressure at which a cavitation cloud was always generated ($P_{cav}=1$) using nanodroplets. In agarose gel, the

Figure 10. A plot of bubble behavior in agarose tissue phantoms. The diameter of bubble generated using a 2-cycle 500kHz pulse at 15MPa as a function of time. At each time point, the average bubble diameter and standard deviation are plotted.

bubble diameter increased to the maximum diameter of 311.2 ± 49.9 μm at 21 μs (*Figure 10*). The average bubble lifespan from the arrival of the histotripsy pulse to when the bubble became too small to be observed on the optical image was measured to be ~60 μs (*Figure 9*). This level of bubble expansion and collapse is similar to the behavior of bubbles formed using histotripsy alone at higher pressures and is anticipated to create cell disruption.
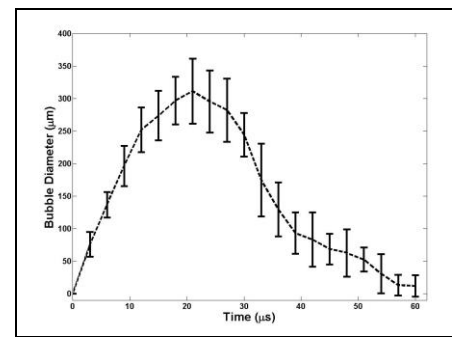
G. Stability of PFP-Loaded Nanodroplets: We investigated the stability of nanodroplets prepared using ABC-1 and ABC-2 polymers and loaded with 2% v/v PFP upon incubation for 24 hours at 37°C in presence and absence of bovine serum albumin (20 µg/ml) as a model serum protein. Using NTA software, we measured the mode and mean size for each formulation at the beginning of the incubation time (0hr) and after 24 hours along with droplets concentration. Results show that the nanodroplets prepared using ABC-1 polymer have an initial mode size and mean size of 131.3±10.9nm and 237.35±6.1nm, respectively (***Figure 11, Panel A***). Incubating the droplets at 37°C for 24 hours caused a slight shift in mode size and mean size to 142.0±10.5nm and 243.9±6.0nm,
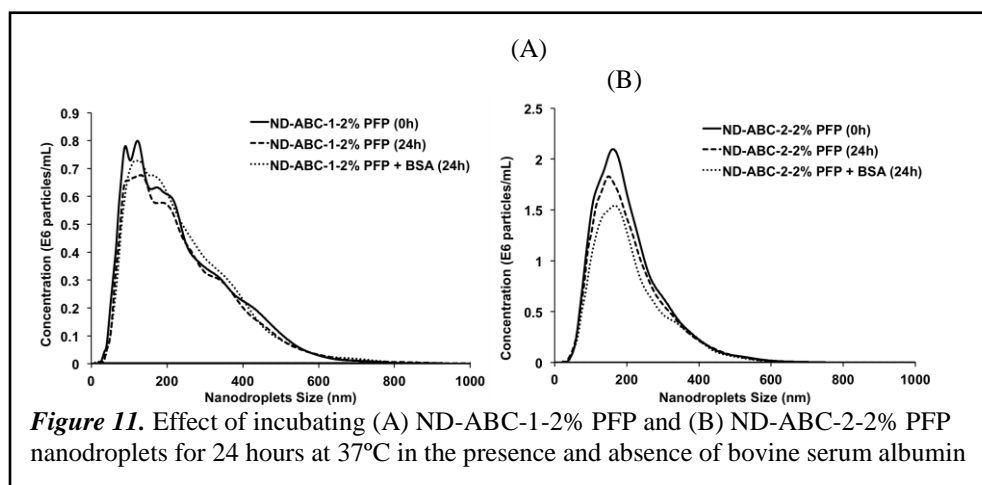

Figure 11. Effect of incubating (A) ND-ABC-1-2% PFP and (B) ND-ABC-2-2% PFP nanodroplets for 24 hours at 37°C in the presence and absence of bovine serum albumin

respectively. Incubating the nanodroplets with BSA did not affect nanodroplets mode size (144.5±13.9nm) and mean size (242.6±4.1nm), which indicates the success of the PEG brush displayed on droplets surface in suppressing BSA adsorption. Results also show that nanodroplets concentration did not change throughout the 24 hours incubation time in presence or absence of BSA, which indicates their stability against dissolution and aggregation. Analysis of mode and mean size of the nanodroplets prepared using ABC-2 and encapsulate 2% v/v PFP show that they maintained their size throughout the incubation time and in presence of BSA (***Figure 11, Panel B***). However, there was a 25% reduction in droplets concentration upon incubation with BSA for 24 hours, which is probably due to droplets dissolution or poor PFP encapsulation indicated by the low ablation capacity of these droplets shown in ***Figure 10***. These results show that ND-ABC-1-2% PFP nanodroplets resist the adsorption of serum proteins and are suited for *in vivo* testing.

To summarize, we have designed and synthesized two amphiphilic PEG-*b*-(PAA)-*b*-P(HDFMA-*co*-MMA) polymers (ABC-1 & ABC-2) that proved to encapsulate 1%-2% v/v PFP forming nanodroplets. Combining histotripsy pulses with nanodroplets formulated using ABC-1 and ABC-2 polymers proved to generate a cavitation bubble cloud that ablates neighboring RBCs at reduced acoustic pressure compared to histotripsy alone. The increase in PFP content from 1% to 2% v/v proved to increase the ablation lesion induced by the nanodroplets. Further, the nanodroplets formulated using ABC-1 appear to better encapsulate the loaded PFP and exhibit higher ablation capacity compared to those formulated by ABC-2 polymer at equal PFP loading. Based on the surface area of the ablation zone, ND-ABC-1-2% PFP nanodroplets exhibit effective ablation of RBCs at 2.5-fold lower acoustic pressure than the intrinsic threshold required initiating the bubble cloud using the same 2-cycle histotripsy pulses alone. Further, these nanodroplets maintained their average size and concentration upon incubation with BSA for 24 hours at 37°C, which prove their promise for cancer cell ablation and warrant their future testing *in vivo*.

Task 2. Investigate the Nanodroplet-Mediated Ultrasound Ablation Phenomena

In task 2, we explored the physical fundamentals of nanodroplet mediated ultrasound ablation in terms of different transducer frequencies, changing the PFC core (PFP vs PFH), and peak negative effect on histotripsy (p-). Briefly, in Task 1 we reported that by use of extremely short, high-pressure pulses, histotripsy cavitation bubbles were generated in regions containing nanodroplets at significantly lower pressure (10.8 MPa) than without nanodroplets (28 MPa) at 500 kHz. In the first study conducting Task 2 we hypothesized that lower frequency would improve the effectiveness of nanodroplet-mediated histotripsy (NMH) by increasing the size of the focal region, increasing bubble expansion, and decreasing the cavitation threshold. In this published study (the original article can be found in Appendix 3), we investigated the effects of ultrasound frequency (345 kHz, 500 kHz, 1.5 MHz, and 3 MHz) on NMH. In the second study to investigate the nanodroplets having a higher boiling point PFC (ie. Perfluorohexane, PFH, 56 °C) other than PFP (29 °C). We hypothesized that nanodroplets with a higher boiling point would remain sustainable cavitation nuclei, allowing cavitation to be maintained over multiple pulses even at low pulse repetition frequency (PRF), which is needed for efficient and complete tissue fractionation via histotripsy. This study is currently under reviewed and the details can be found in Appendix 4. The third study is related to investigation of the negative pressure (p-) effect which assumed cavitation nucleation is caused by the negative pressure (p-) exposed to the PFC, as predicted by classical nucleation theory, and the NMH cavitation threshold is therefore determined by the incident p- of the single-cycle pulses commonly used in NMH. The findings of this study is also under reviewed that can be seen as Appendix 5.
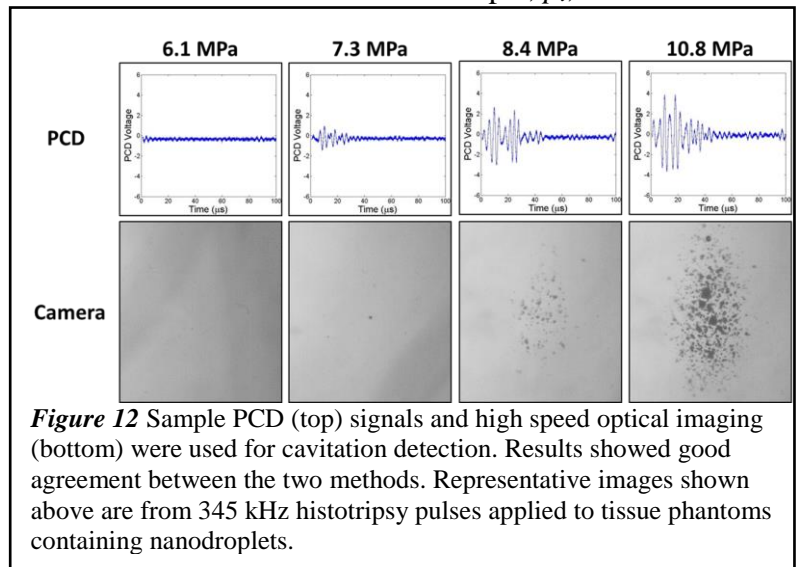
1. *Frequency Study*

A. NMH Cavitation Threshold: For cavitation threshold experiments, 100 pulses were applied inside each sample at each pressure level at a pulse repetition frequency (PRF) of 0.5 Hz. The PRF was kept low to minimize the possibility that cavitation from one pulse would change the probability of cavitation on a subsequent pulse. In a previous study, it was demonstrated that cavitation during a pulse increased the likelihood of cavitation on a following pulse for PRFs > 1 Hz, , but this effect was not observed for PRFs below 1 Hz [15]. In addition to this low PRF, the focus was translated for each pulse by 1 mm transverse to the acoustic propagation direction in a 10×10 grid in order to minimize the effects of cavitation damage to the nanodroplets or tissue phantom sample from altering the probability of cavitation. For each pulse, cavitation was monitored using both high speed imaging and PCD, and the fraction of total pulses (out of 100) for which cavitation was detected was determined as the cavitation probability.

The probability of observing cavitation followed a sigmoid function, given by

$$P(p_-) = \frac{1}{2} + erf\left(\frac{p_- - p_t}{\sqrt{2\sigma^2}}\right) \text{ (E1)}$$

where *erf* is the error function, p_t is the negative pressure at which the probability $p_{cav}=0.5$, σ is a variable related to the width of the transition between $p_{cav}=0$ and $p_{cav}=1$, with $\pm \sigma$ giving the difference in pressure from about $p_{cav}=0.15$ to $p_{cav}=0.85$ for the fit [15]. The cavitation threshold for each sample, p_t, is defined as the p- corresponding to $p_{cav}=0.5$ as calculated by the curve fit. Curve fitting for all data sets was performed using an OriginLab curve fitting program (OriginPro 9.1; OriginLab Corporation, Northampton, MA, USA). The fit curves for all samples were analyzed statistically to determine whether the differences in the values of p_t were significantly different from each other. The standard errors for p_t were estimated by a covariance matrix using the delta method [16]. The curves were compared using a two-sample t-test with statistic

$t\left(p_{int1} - p_{int2}, \sqrt{SE_1^2 + SE_2^2}\right)$ at a 95% confidence interval. Results were considered

Figure 12 Sample PCD (top) signals and high speed optical imaging (bottom) were used for cavitation detection. Results showed good agreement between the two methods. Representative images shown above are from 345 kHz histotripsy pulses applied to tissue phantoms containing nanodroplets.

statistically significant for p<0.05. Note that the standard error does not include the uncertainty in absolute pressure from the hydrophone measurement, only the uncertainty in the fit, because the values p_t are relative. A sample size of 3 tissue phantoms was used for each experimental condition.

To investigate the effects of ultrasound frequency on the NMH threshold, histotripsy pulses were applied to tissue-mimicking agarose phantoms with and without nanodroplets using the 345 kHz, 500 kHz, 1.5 MHz, and 3 MHz histotripsy transducers. For all frequencies, cavitation bubbles were observed on the high-speed camera in an increasingly larger area with increasing pressure when a certain negative pressure was exceeded, with close agreement between optical imaging and PCD detection methods (**Figure 12**), as seen in previous studies[15, 17]. Results from phantoms without nanodroplets show that the histotripsy intrinsic threshold, p_{t_int}, was between p_{t_int} = 23.7−25.9 MPa, with σ_{mean} = 2.0 MPa for 345 kHz; p_{t_int} = 23.5−26.7 MPa, with σ_{mean} = 1.8 MPa for 500 kHz; p_{t_int} = 26.3−27.0 MPa, with σ_{mean} = 1.0 MPa for 1.5 MHz; and p_{t_int} = 26.3−27.2 MPa, with σ_{mean} = 0.9 MPa for 3 MHz (**Figure 13**). Note that at lower amplitudes, cavitation was occasionally observed that deviated from the curve function, especially at lower frequency. These cavitation events were probably caused by contamination of the sample by heterogeneities in the liquid that could not be entirely avoided throughout the experiment. The effects of nanodroplets on the cavitation threshold demonstrated a significant decrease in the cavitation threshold compared to the histotripsy intrinsic threshold. Results from agarose phantoms

Figure 13 Cavitation threshold curves. Probability curves for tissue phantoms with and without nanodroplets. Results showed a significant decrease in the cavitation threshold with nanodroplets compared to controls. Results also showed a significant increase in the nanodroplet cavitation threshold with increasing frequency.

with PFP nanodroplets show that the NMH threshold, p_{t_PFP}, was between p_{t_PFP} = 7.3−7.4 MPa, with σ_{mean} = 1.4 MPa for 345 kHz; p_{t_PFP} = 8.2−10.0 MPa, with σ_{mean} = 0.8 MPa for 500 kHz; p_{t_PFP} = 10.3−10.7 MPa, with σ_{mean} = 0.4 MPa for 1.5 MHz; and p_{t_PFP} = 12.9−13.7 MPa, with σ_{mean} = 0.6 MPa for 3 MHz (**Figure 13**). The results of the cavitation threshold for all frequencies are plotted in **Figure 14**. Comparing the results for the NMH threshold and histotripsy intrinsic threshold demonstrated a significant decrease in the cavitation threshold and a significant increase in the steepness of the S-curve (σ) for samples containing nanodroplets at all frequencies. Additionally, it was observed that the NMH threshold was significantly decreased at lower frequency (**Figure 14**).
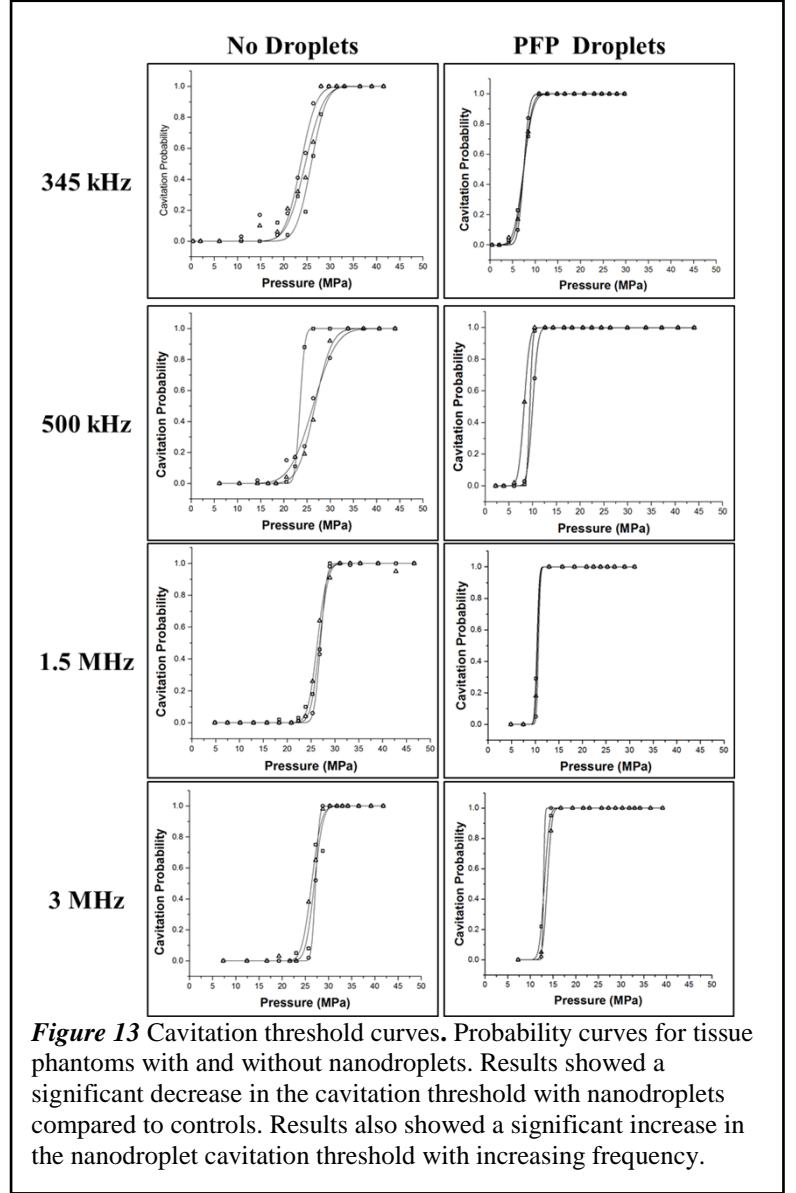
B. _**NMH Bubble Size:**_ To determine if nanodroplet-mediated cavitation bubbles were expanded similar to histotripsy bubbles at higher pressure, optical images of the growth and collapse of bubbles were recorded by the high-speed camera. Nanodroplet-mediated cavitation bubbles were generated by the 345 kHz, 500 kHz, 1.5 MHz, and 3 MHz transducers at peak negative pressures slightly above the nanodroplet cavitation threshold at each frequency. More specifically, the peak negative pressure was 10.8 MPa (345 kHz), 10.3 MPa (500 kHz), 12.9 MPa (1.5 MHz), and 14.7 MPa (3 MHz). For comparison, bubbles were produced in tissue phantoms without nanodroplets at estimated peak negative pressures of 26.4 MPa (345 kHz), 26.3 MPa (500 kHz), 26.8 MPa (1.5 MHz), and 28.8 MPa (3 MHz), which is slightly above the intrinsic threshold without nanodroplets.

The maximum radius of bubbles was compared by reconstructing the average expansion and collapse behavior using a series of time-delayed images of the bubbles produced by identical histotripsy pulses. The specific delay times were varied based on the frequency and sample in order to reconstruct a sequence of bubble images and determine the time point corresponding to the maximum bubble radius, R_{max}. The R_{max} was compared between samples by analyzing results from 20 identical histotripsy pulses recorded at the time of maximum expansion, with each pulse applied to a different point in the sample (2 mm spacing) to prevent the effects of cavitation damage from altering the tissue phantom and nanodroplet properties. The size of single bubbles was measured for all twenty pulses to determine the bubble radius, and the mean and standard deviation in bubble radius was calculated. The calculated values for $R_{max} \pm$ the standard deviation were compared for tissue phantoms with and without nanodroplets exposed to histotripsy pulses at 345 kHz, 500 kHz, 1.5 MHz, and 3 MHz. A sample size of 6 tissue phantoms was used for each experimental condition. To study the effects of ultrasound frequency on the expansion of NMH bubbles, the maximum bubble radius, R_{max}, produced by 345 kHz, 500 kHz, 1.5 MHz, and 3 MHz histotripsy pulses was measured in phantoms with and without nanodroplets. The peak negative pressure used for each frequency was chosen to be slightly above the cavitation threshold at each frequency so that cavitation was always generated (P_{cav}=1). Optical imaging results demonstrated that NMH bubbles were significantly smaller than histotripsy bubbles generated above the intrinsic threshold (**Figure 15**). At all frequencies, results showed that the R_{max} for NMH bubbles was between 30%-40% of the R_{max} measured for histotripsy bubbles produced above the intrinsic threshold (**Figure 16**). Results further showed that larger bubbles were observed at lower frequency for both the histotripsy only and NMH conditions (**Figure 17**).
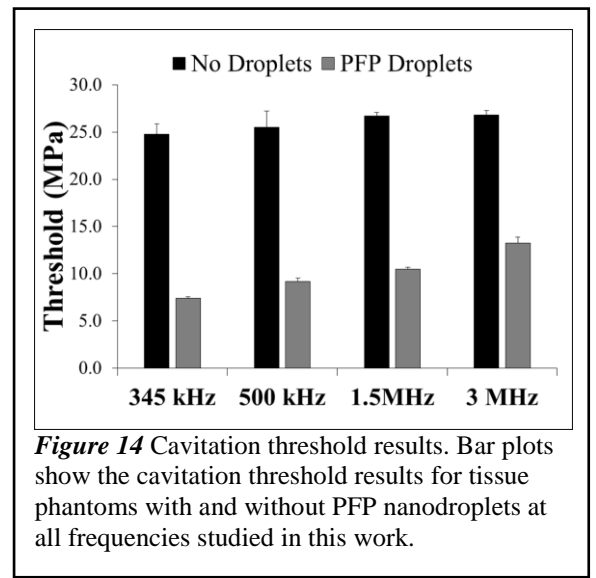

Figure 14 Cavitation threshold results. Bar plots show the cavitation threshold results for tissue phantoms with and without PFP nanodroplets at all frequencies studied in this work.
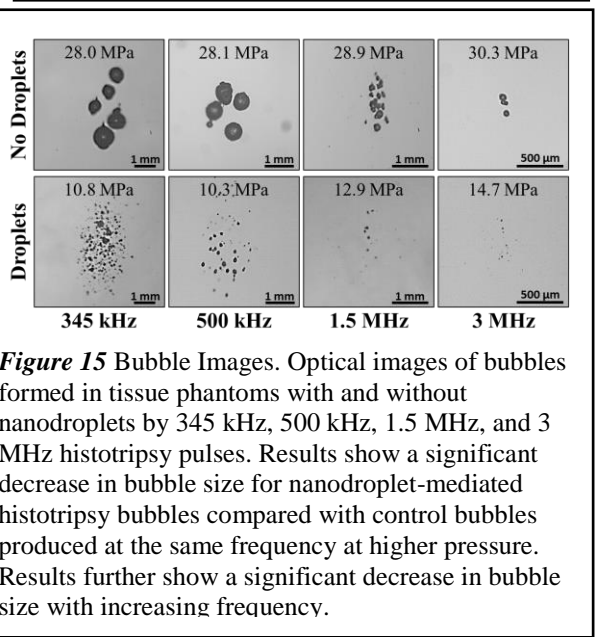

Figure 15 Bubble Images. Optical images of bubbles formed in tissue phantoms with and without nanodroplets by 345 kHz, 500 kHz, 1.5 MHz, and 3 MHz histotripsy pulses. Results show a significant decrease in bubble size for nanodroplet-mediated histotripsy bubbles compared with control bubbles produced at the same frequency at higher pressure. Results further show a significant decrease in bubble size with increasing frequency.
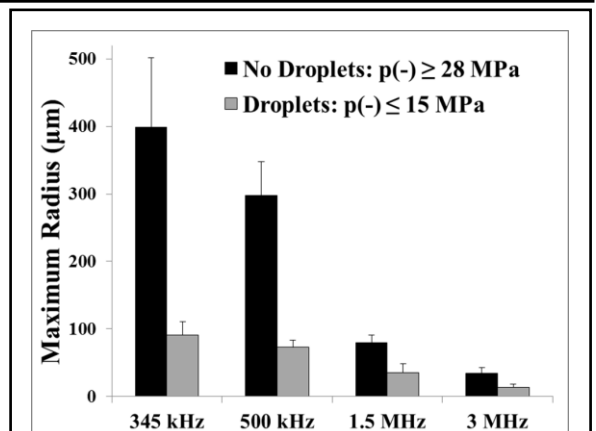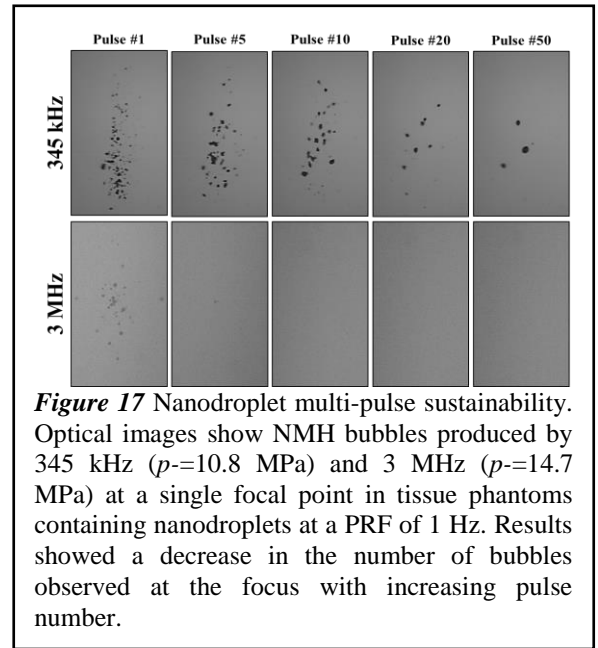

Figure 16 Bubble R_{max} results. Plot shows a comparison of the maximum bubble radius produced in tissue phantoms with and without nanodroplets by 345 kHz, 500 kHz, 1.5 MHz, and 3 MHz histotripsy pulses. The peak negative pressure applied for each condition are listed in Table 2. rther show a significant decrease in bubble size with increasing frequency.

For example, R_{max} for NMH bubbles was shown to decrease from 126.7±47.2 µm at 345 kHz to 106.5±17.6 µm, 34.7±13.4 µm, and 12.9±5.3 µm at 500 kHz, 1.5 MHz, and 3 MHz, respectively (**Figure 16**). Comparing R_{max} for NMH and histotripsy bubbles showed that, although NMH bubbles were significantly smaller than histotripsy bubbles for all frequencies, NMH bubbles produced at lower frequency grew larger than histotripsy bubbles produced at higher frequency. For example, the R_{max} of NMH bubbles produced at 345 kHz and 500 kHz (126.7±102.5 µm and 106.5±17.6 µm) were significantly larger than the R_{max} of histotripsy bubbles generated above the intrinsic threshold at 1.5 MHz and 3 MHz (79.5±11.5µm and 34.3±8.5) (**Figure 16**).

C. NMH Multi-pulse Sustainability: To determine if nanodroplets are sustainable cavitation nuclei over multiple pulses, 1000 ultrasound pulses were applied to a single focal region in tissue phantoms containing nanodroplets at a PRF of 1 Hz and peak negative pressures of 10.8 MPa (345 kHz), 10.3 MPa (500 kHz), 12.9 MPa (1.5 MHz), and 14.7 MPa (3 MHz). In a previous study, nanodroplet-mediated histotripsy created consistent, well-defined fractionation in tissue phantoms at 10 Hz PRF by maintaining cavitation at over multiple pulses[18]. However, it is unclear whether the nanodroplets themselves or the residual nuclei from previous pulses are responsible for seeding cavitation after the first few pulses. As a result, the PRF in this study was kept low (1 Hz) to minimize the contributions of residual nuclei from a previous pulse from effecting cavitation generation on a subsequent pulse in order to determine if nanodroplets continue to function as viable cavitation nuclei after the first few pulses or if the nanodroplets are destroyed in the cavitation process. Cavitation was monitored using high speed optical imaging, and the number of bubbles produced by each pulse was compared for 1000 histotripsy pulses in each sample.To determine if nanodroplets are sustainable cavitation nuclei over multiple pulses, 1000 histotripsy pulses were applied to a single focal region in phantoms containing nanodroplets at a PRF of 1 Hz. Results demonstrated that a bubble cloud consisting of many bubbles was observed after the first pulse (**Figure 17**). However, the number of bubbles observed inside the cloud significantly decreased with increasing number of pulses (**Figure 17**). For example, only one bubble was observed after 5 pulses at 3 MHz, with no bubbles remaining after 10 pulses (**Figure 17**). At lower frequency, bubbles were generated for more pulses than at higher frequency, but still showed the same trend of decreasing number of bubbles with increasing pulse number (**Figure 17**). It is likely that bubbles lasted for more pulses at lower frequency due to enhanced bubble expansion resulting in a larger population of residual nuclei and a corresponding increase in dissolution time. For all frequencies, no bubbles were observed after 100 pulses were applied to the sample.

Figure 17 Nanodroplet multi-pulse sustainability. Optical images show NMH bubbles produced by 345 kHz (*p*-=10.8 MPa) and 3 MHz (*p*-=14.7 MPa) at a single focal point in tissue phantoms containing nanodroplets at a PRF of 1 Hz. Results showed a decrease in the number of bubbles observed at the focus with increasing pulse number.
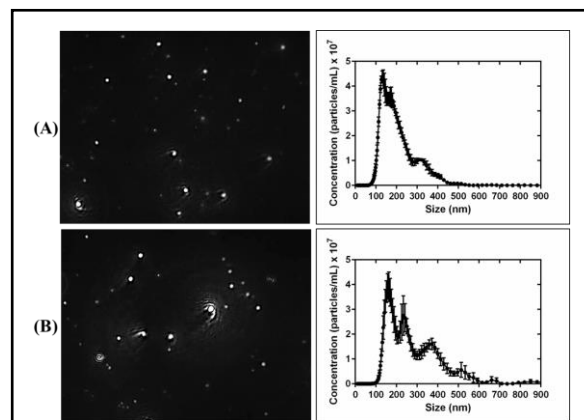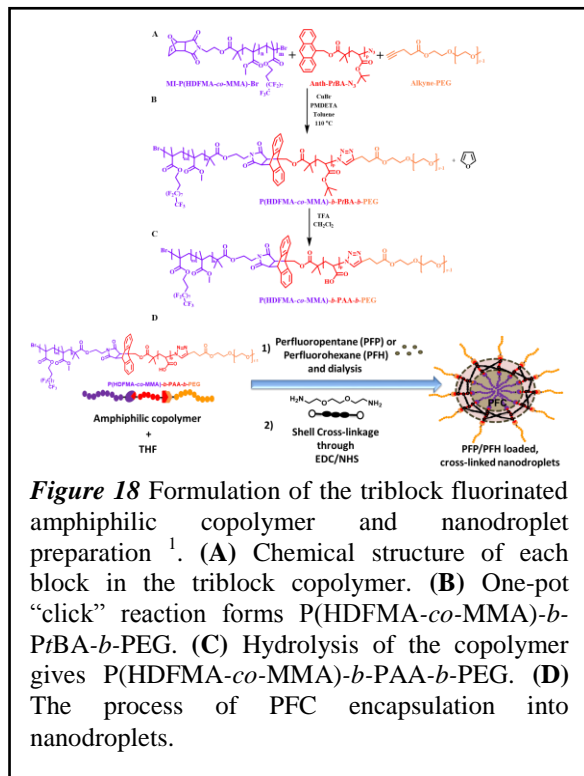
In this work, the effects of ultrasound frequency on nanodroplet-mediated histotripsy were investigated, with results supporting our hypothesis that lower frequency will improve the effectiveness of NMH therapy. Results demonstrated that the NMH threshold was significantly reduced at lower frequency, ranging from 7.4 MPa at 345 kHz to 13.2 MPa at 3 MHz. Furthermore, results demonstrated that NMH bubble expansion was enhanced at lower frequency, generating bubbles with a maximum radius >100 µm despite the reduced pressure applied. Finally, multi-pulse experiments demonstrated that nanodroplets are destroyed during the first few pulses at 1Hz PRF, suggesting that higher PRF treatments or nanodroplets with a higher boiling point may be required in order to maintain an NMH bubble cloud over multiple pulses. Overall, the results of this study provide significant insight in the role of ultrasound parameters in NMH therapy and will provide a rational basis to specifically tailor acoustic parameters in order to improve NMH tissue fractionation.

2. *PFC Composition Study*

A. <u>Nanodroplet Characterization:</u> A well-defined, triblock amphiphilic copolymer containing a hydrophilic poly(ethylene glycol) (PEG) block, a middle block poly(acrylic acid) (PAA) block, and a hydrophobic random copolymer of heptadecafluorodecyl methacrylate (HDFMA) and methyl methacrylate (MMA) was engineered using a combination of atom transfer radical polymerization (ATRP) and "click" coupling techniques as previously described (**Figure 18**) [1]. The synthesis of the P(HDFMA-*co*-MMA)-*b*-PAA-*b*-PEG triblock copolymer is shown in Figure 1, and described in detail in our previous study [1]. The synthesized P(HDFMA$_8$-*co*-MMA$_{20}$)-*b*-PAA$_{12}$-*b*-PEG$_{45}$ triblock amphiphilic copolymer was used to prepare PFP- and PFH-loaded nanodroplets. Briefly, the copolymers were dissolved in tetrahydrofuran (THF) (0.2% w/v) and cooled down to 0 $^\circ$C before the addition of PFP (2% v/v) or PFH (2% v/v) while vigorously stirring in the copolymer-perfluorocarbon mixture. An equal amount of purified water was drop-wise added to this solution mixture to initiate micelle formation and the mixture was stirred for 1h in an ice bath. The micelles solution was transferred into a dialysis bag (MWCO of 1 KDa, Spectrum, Rancho Dominguez, CA, US) and

Figure 18 Formulation of the triblock fluorinated amphiphilic copolymer and nanodroplet preparation [1]. (**A**) Chemical structure of each block in the triblock copolymer. (**B**) One-pot "click" reaction forms P(HDFMA-*co*-MMA)-*b*-P*t*BA-*b*-PEG. (**C**) Hydrolysis of the copolymer gives P(HDFMA-*co*-MMA)-*b*-PAA-*b*-PEG. (**D**) The process of PFC encapsulation into nanodroplets.

dialyzed against ice-cold MES solution of pH 5.5 during overnight to remove the THF and get a milky solution of non-cross-linked PFP-loaded nanodroplets and non-cross-linked PFH-loaded nanodroplets. Each nanodroplet in the milky solution was transferred to a round bottom flask and mixed with the 2,2`-(ethylenedioxy)-bis(ethylamine) cross-linker, which reacts with the carboxyl groups of the central PAA block in the copolymer via NHS/EDC coupling chemistry forming cross-linked nanodroplets with a flexible polymer shell. Shell cross-linked nanodroplets were dialyzed against ice-cold water for 12 hours to remove unreacted cross-linker debris with byproducts of the reaction. Concentration and size distribution of the nanodroplets were measured using Nanoparticle Tracking Analysis (NTA). In this study, we aimed to encapsulate PFH into a P(HDFMA-*co*-MMA)-*b*-PAA-*b*-PEG fluorinated copolymer synthesized in-house in order to compare the cavitation ability of PFH-loaded nanodroplets with PFP-loaded nanodroplets. In our previous study, we demonstrated that PFP can be encapsulated in the fluorinated copolymer, forming nanodroplets containing an elastic shell with an average size of ~100-400 nm [1]. In contrast to PFP, the solubility of PFH is limited in most common polar solvents as well as water. Moreover, when PFH is added to any of these solvents, it is not dissolved and leads to phase-separation from the solvent. In this study, we hypothesized that PFH could be homed with the same fluorinated copolymer formulation of P(HDFMA-*co*-MMA)-*b*-P*t*BA-*b*-PEG in order to form nanodroplets with similar size and characteristics to the PFP droplets synthesized in our previous study [1]. Results demonstrated that both PFP and

Figure 19 Nanoparticle Tracking Analysis (left) demonstrated similar characteristics for (**A**) PFP and (**B**) PFH nanodroplets. Size distribution plots (right) show the average size of the droplets was 177.9±1.9 nm and 233.9±3.9 nm for PFP and PFH, respectively.

PFH encapsulated into stable nanodroplets in the desired size range (100-600 nm). NTA size analysis showed similar characteristics for the PFP and PFH droplets (**Figure 19**). PFP-loaded nanodroplets size ranged from 100-450 nm with the major peak <300 nm. The size distribution of PFH-loaded nanodroplets was slightly larger than the PFP-loaded ones, ranging from 00-600 nm. Three additional high-intense peaks in the range of 200-300 nm, 300-450 nm, and 450-600 nm were observed in the large size portion of the

PFH nanodroplet size plot (**Figure 19B**). The larger size of the PFH-loaded nanodroplets is possibly due to the miscibility character differences between PFP and PFH in the THF/copolymer mixture. For example, PFP was observed to homogenously dispense in the THF/copolymer mixture in the beginning of particle preparation, whereas PFH remained separate from the mixture on the bottom of the round-bottom flask. This energetically favorable phase separation was broken by adding water in drop-wise to trigger the micellization process of the amphiphilic copolymer under vigorous stirring. This strategy allowed for the unmixed PFH in the mixture to be made miscible in the aqua system due to the fluorinated-hydrophobic and hydrophilic polymer contents of the amphiphilic copolymer. Both types of droplets were dispersed throughout the medium, and neither droplet type was observed to aggregate together due to the amphiphilic character of the triblock copolymer that stabilized the perfluorocarbons in the core of the nanodroplets as well as enhanced the solubility of the particles with the contribution of hydrophilic PEG corona. Nanodroplet concentration and size characterization demonstrated similar size distributions for the PFP and PFH nanodroplets (**Figure 19**). The error bars on the size distribution plots represent the standard deviation of the repeat measurements of each sample. The mean size and standard deviation values obtained by the NTA software correspond to arithmetic values calculated with the sizes of all particles analyzed for each sample (n=5). Results from all samples demonstrated an average size of 177.9±1.9 nm and 233.9±3.9 nm for PFP and PFH nanodroplets, respectively.

The results from the nanodroplet characterization suggest that the droplet preparation method described by us can be used to create nanodroplets with similar surface characteristics within the media while the composition of the encapsulated perfluorocarbon can be modulated as desired [1]. The design of the triblock amphiphilic copolymer acts to increase the particle's solubility in aqueous environments due the hydrophilic character of the outer PEG block while also improving hemocompatibility (i.e. no protein adsorption on the particles, no macrophage recognition, and minimum interaction with blood cells during blood circulation) [1, 19]. The results of this study suggest that the PFC inside the nanodroplets can be easily modified to take advantage of different boiling point perfluorocarbons without losing the benefits of the functionalized polymer shell. Being able to independently alter the droplet parameters without affecting the engineered nanodroplet particle offers significant advantages for optimizing NMH therapy, allowing for the development of droplets with varying boiling points that maintain the same targeting behavior for NMH tumor therapy. This desired targeting behavior includes having nanodroplets in the optimal size range for passive targeting through the leaky tumor vasculature (100-800 nm) as well as having the functionalized particles for active targeting to tumor cells or other diseased lesions using targeting ligands [20 21].

B. NMH Cavitation Threshold For cavitation threshold experiments, 100 pulses were applied inside each sample at each pressure level at a pulse repetition frequency (PRF) of 0.5 Hz. The PRF was kept low to minimize the possibility that cavitation from one pulse would change the probability of cavitation on a subsequent pulse. In a previous study, it was demonstrated that cavitation during a pulse increased the likelihood of cavitation on a following pulse for PRFs > 1 Hz, , but this effect was not observed for PRFs < 1 Hz [15]. In addition to this low PRF, the focus was translated for each pulse by 1 mm transverse to the acoustic propagation direction in a 10×10 grid in order to minimize the effects of cavitation damage to the nanodroplets or tissue phantoms from altering the probability of cavitation. For each pulse, cavitation was monitored using both high speed imaging and PCD, and the fraction of total pulses (out of 100) for which cavitation was detected was determined as the cavitation probability.

The probability of observing cavitation followed a sigmoid function, given by

$$P(p_-) = \frac{1}{2} + erf\left(\frac{p_- - p_t}{\sqrt{2\sigma^2}}\right) \quad \text{(E1)}$$

where *erf* is the error function, p_t is the negative pressure at which the probability p_{cav}=0.5, σ is a variable related to the width of the transition between p_{cav}=0 and p_{cav}=1, with $\pm \sigma$ giving the difference in pressure from about p_{cav}=0.15 to p_{cav}=0.85 for the fit [15]. The cavitation threshold for each sample, p_t, is defined as the p- corresponding to p_{cav}=0.5 as calculated by the curve fit. Curve fitting for all data sets was performed using an OriginLab curve fitting program (OriginPro 9.1; OriginLab Corporation, Northampton, MA, USA). The fit curves for all samples were analyzed statistically to determine whether the differences in the values of p_t were significantly different from each other. The standard errors for p_t were estimated by a covariance

matrix using the delta method [16]. The curves were compared using a two-sample t-test with statistic $t\left(p_{int1} - p_{int2}, \sqrt{SE_1^2 + SE_2^2}\right)$ at a 95% confidence interval. Results were considered statistically significant for p<0.05. Note that the standard error does not include the uncertainty in absolute pressure from the hydrophone measurement, only the uncertainty in the fit, because the values p_t are relative. A sample size of 3 tissue phantoms was used for each experimental condition (i.e. PFP nanodroplets, PFH nanodroplets, or no nanodroplets).To investigate the effects of nanodroplet composition on the NMH threshold, histotripsy pulses were applied to tissue-mimicking agarose phantoms with PFP nanodroplets, PFH nanodroplets, and no nanodroplets using the 345 kHz, 500 kHz, 1.5 MHz, and 3 MHz histotripsy transducers. For all experimental conditions, cavitation bubbles were observed on the high-speed camera in an increasingly larger area with increasing pressure once a certain negative pressure was exceeded, with close agreement between optical imaging and PCD detection methods (**Figure 20**), as seen in previous studies [15, 22]. Plotting the probability of cavitation as a function of peak negative pressure demonstrated a significant decrease in the cavitation threshold with both PFP and PFH nanodroplets compared to controls at all frequencies (**Figure 21**). Additionally, results showed a slight increase in the nanodroplet cavitation threshold for PFH nanodroplets compared to PFP nanodroplets (**Figure 21**). Comparing the threshold results for phantoms containing PFH nanodroplets with control phantoms demonstrated that the cavitation threshold was decreased by 14.4 MPa, 15 MPa, 13.7 MPa, and 11.9 MPa at 345 kHz, 500 kHz, 1.5 MHz, and 3 MHz, respectively (**Figure 22**). When comparing phantoms containing PFP and PFH nanodroplets (**Figure 22**), a decrease of 3 MPa, 1.3 MPa, 2.5 MPa, and 1.7 MPa was observed for PFP phantoms at 345 kHz, 500 kHz, 1.5 MHz, and 3 MHz, respectively (**Figure 22**). For all experimental conditions, the cavitation threshold was observed to decrease at lower frequency, as has been observed in previous studies (**Figure 22**)[18, 22].
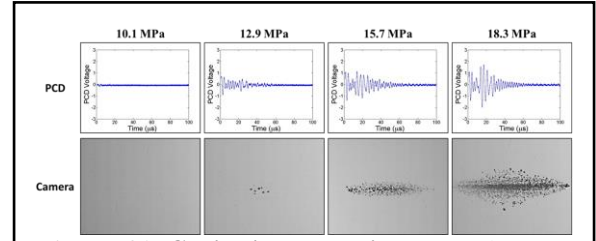

Figure 20 **Cavitation detection.** Sample PCD signals (top) and high speed optical imaging (bottom) were used for cavitation detection for cavitation threshold experiments. Results showed good agreement between the two methods.
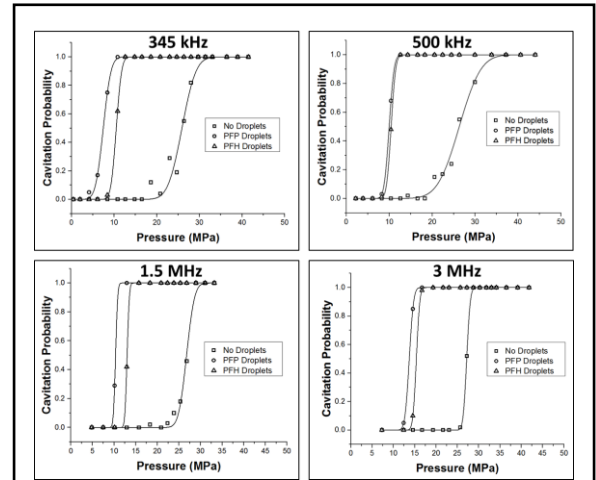

Figure 21 **Sample cavitation threshold curves.** Plots show sample probability curves for tissue phantoms containing PFP nanodroplets, PFH nanodroplets, and no nanodroplets at 345 kHz, 500 kHz, 1.5 MHz, and 3 MHz.

The experimental results for the cavitation threshold experiments support our hypothesis that both PFP and PFH nanodroplets can be used to significantly reduce the pressure required to generate histotripsy bubbles for NMH therapy. At all frequencies tested, the NMH threshold for both types of droplets was significantly lower (>10 MPa decrease) than the histotripsy intrinsic threshold, while maintaining a steep threshold behavior. In fact, the σ_{mean} values calculated by the curve fit decreased (i.e. sharper threshold curve) for phantoms containing nanodroplets, with the lowest σ_{mean} values observed for phantoms containing PFH droplets. This distinct threshold behavior is promising for the development of NMH therapy in which the applied pressure must be chosen in the region above the NMH threshold but below the histotripsy intrinsic threshold to ensure cavitation is only generated in regions containing nanodroplets. The results of these threshold experiments suggest that both PFP and PFH nanodroplets could be used
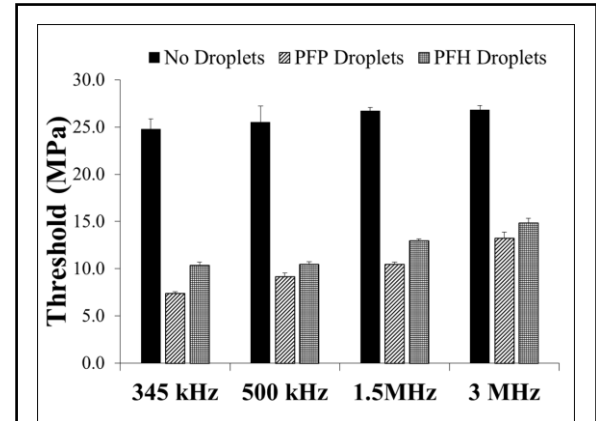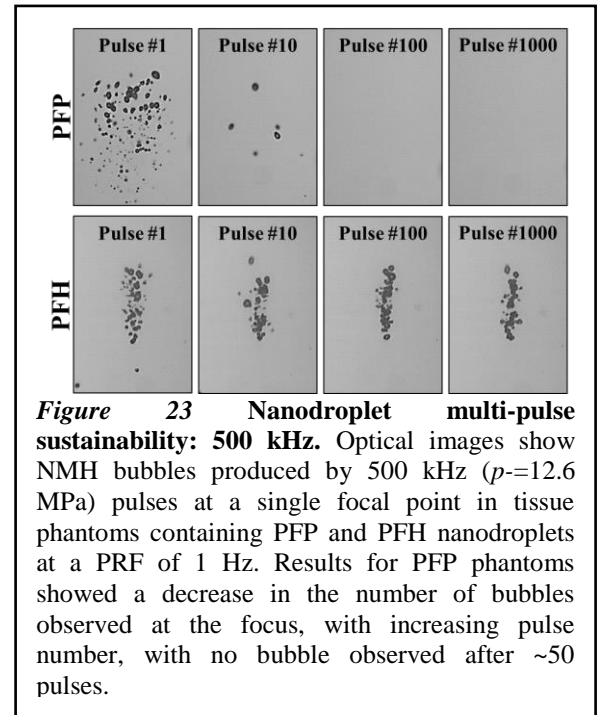

Figure 22 **Cavitation threshold results.** Bar plots show the complete cavitation threshold results for tissue phantoms containing PFP nanodroplets, PFH nanodroplets, and no

for NMH, with PFP droplets offering a slightly lower threshold (~1-3 MPa decrease). With everything else equal, one might expect a lower cavitation threshold for the larger PFH droplets (233.9±3.9 nm) compared to PFP droplets (177.9±1.9 nm). It is possible that the slight decrease in threshold for PFP droplets is due to the lower surface tension of PFP (9.5 mN/m) compared to PFH (1.2 mN/m), as previous work has demonstrated that the cavitation threshold is highly dependent upon the surface tension of the media when using the 1-2 cycle pulses used in this study [15, 22]. These results suggest that the nanodroplets may actually decrease the cavitation threshold by carrying a lower threshold medium, rather than each droplet acting as single cavitation nuclei as would be the case for an air contrast agent. Based on this finding, the results of this work suggest that the NMH threshold can be selectively modulated by changing the droplet composition, with lower surface tension resulting in a decreased cavitation threshold. The finding that the NMH threshold can be finely tuned by changing droplet composition while maintaining the distinct threshold behavior is a significant benefit for the development of NMH therapy as well as for other nanodroplet applications such as selective drug delivery drug delivery [23].

C. <u>NMH Multi-pulse Sustainability:</u> To test the hypothesis that PFH nanodroplets will remain sustainable cavitation nuclei over multiple pulses while PFP nanodroplets will be destroyed during the first few pulses, 1000 ultrasound pulses were applied to a single focal region in tissue phantoms containing PFP and PFH nanodroplets at a PRF of 1 Hz and peak negative pressures of 11.8 MPa (345 kHz), 12.6 MPa (500 kHz), 14.3 MPa (1.5 MHz), and 15.6 MPa (3 MHz). The PRF in this study was kept low (1 Hz) to minimize the contributions of residual nuclei from a previous pulse from effecting cavitation generation on a subsequent pulse in order to determine if PFP and PFH nanodroplets continue to function as viable cavitation nuclei after the first few pulses or if the nanodroplets are destroyed in the cavitation process. Furthermore, a PRF of 1 Hz was also chosen as previous work has shown an increase in ablation efficiency for 1 Hz treatments in comparison to higher PRF treatments that rely on residual nuclei from previous pulses to maintain the cavitation bubble cloud[24]. Cavitation was monitored using high speed optical imaging, and the number of bubbles produced by each pulse was compared for 1000 histotripsy pulses in each sample. To compare the ability of nanodroplets to act as sustainable cavitation nuclei over multiple pulses, 1000 histotripsy pulses were applied to a single focal region in phantoms containing PFP and PFH nanodroplets at a PRF of 1 Hz. Results demonstrated that a bubble cloud consisting of many bubbles was observed after the first pulse for both types of droplets (**Figure 23**). However, the bubble cloud generated in PFH phantoms was a more well-defined bubble cloud, similar to those previously observed for histotripsy above the intrinsic threshold [22, 25]. At all frequencies, over all 1,000 pulses, a dense bubble cloud was produced in PFH phantoms, with the bubbles more tightly confined inside the focal region and no significant change in the number of bubbles inside the cloud. In comparison, after the first pulse, the bubble cloud generated in the PFP phantom is sparsely populated. At all frequencies, the number of bubbles observed inside PFP phantoms significantly decreased with increasing number of pulses, and bubbles distinguished after ~5-50 pulses. At a higher frequency, the bubble cloud distinguished with fewer number of pulses. For example, no bubbles were observed after ~50 pulses in PFP phantoms exposed to 500 kHz (*p*-=12.6 MPa) pulses and after ~5 pulses exposed to 3 MHz (*p*-=15.6 MPa) pulses.

Figure 23 Nanodroplet multi-pulse sustainability: 500 kHz. Optical images show NMH bubbles produced by 500 kHz (*p*-=12.6 MPa) pulses at a single focal point in tissue phantoms containing PFP and PFH nanodroplets at a PRF of 1 Hz. Results for PFP phantoms showed a decrease in the number of bubbles observed at the focus, with increasing pulse number, with no bubble observed after ~50 pulses.

The finding that PFH nanodroplets act as sustainable cavitation nuclei over multiple pulses, while PFP droplets are destroyed during the initial pulses, supports our hypothesis that using droplets with a higher boiling point is advantageous for NMH therapy. Results suggest that PFH droplets may re-condense into a liquid after the collapse of the cavitation bubble while the PFP bubbles are destroyed by the cavitation process (i.e. do not return to liquid form). These results suggest that higher boiling point droplets can be

used to significantly reduce the nucleation threshold for generating cavitation bubbles over multiple pulses, allowing NMH therapy to be applied for multiple pulses until the targeted tissue is completely fractionated, even at low PRF. These results suggest that, due to the lower boiling point, PFP nanodroplets are only capable of reducing the cavitation threshold on the initial pulses, requiring cavitation on subsequent pulses to be generated from residual nuclei remaining in the focal region from previous pulses. The finding that higher boiling point droplets can serve as functional cavitation nuclei over multiple pulses is therefore a major benefit for NMH therapy, as previous work has shown a decrease in ablation efficiency for higher PRF treatments that rely on residual nuclei from previous pulses to maintain the cavitation bubble cloud [24a]. In addition to the finding that PFH droplets acted as sustainable cavitation nuclei over multiple pulses, it was also observed that the NMH bubble clouds produced from PFH droplets were more well-defined and densely populated compared to the sparse bubble clouds produced by the PFP droplets, even when comparing bubble clouds produced on the first pulse. The well confined, dense bubble clouds produced inside the PFH phantoms closely match the behavior of bubble clouds previously observed for histotripsy treatments above the intrinsic threshold, which have been shown to be efficient and precise at fractionating the target tissue [15, 22, 24b, 25]. In contrast, the more sparse bubble clouds produced inside the PFP phantoms resemble bubble clouds generated at higher PRF or bubble clouds that rely upon residual nuclei in order to maintain cavitation, which have been shown to be less efficient at fractionating tissue while increasing collateral damage to surrounding tissue [24a]. This observation suggests that NMH bubble clouds produced using PFH droplets will be more efficient at fractionating tissue and provide less collateral damage to surrounding tissue compared to NMH therapy using PFP droplets.

In this work, the effects of droplet composition on NMH therapy were investigated using perfluoropentane (boiling point~29°C, surface tension~9.5 mN/m) and perfluorohexane (boiling point~56°, surface tension~1.2 mN/m) droplets. The results demonstrated a significant decrease in the cavitation threshold for both types of nanodroplets compared to controls, with a slightly lower threshold observed for PFP phantoms, likely due to the decrease in surface tension for PFP. Results further demonstrated that PFH nanodroplets were sustainable cavitation nuclei over multiple pulses, while PFP nanodroplets were destroyed during the initial pulses. This effect is most likely due to the re-condensing of PFH droplets into a liquid after the cavitation event occurs, due to the higher boiling point of the PFH droplets. The results of this study suggest that NMH therapy can be significantly enhanced by modulating droplet composition in order to optimize the cavitation threshold (decrease droplet surface tension) and increase the multi-pulse sustainability (increase droplet boiling point). Overall, the results of this study provide significant insight in the role of droplet composition in NMH therapy and will provide a rational basis to specifically tailor droplet parameters in order to improve NMH tissue fractionation.
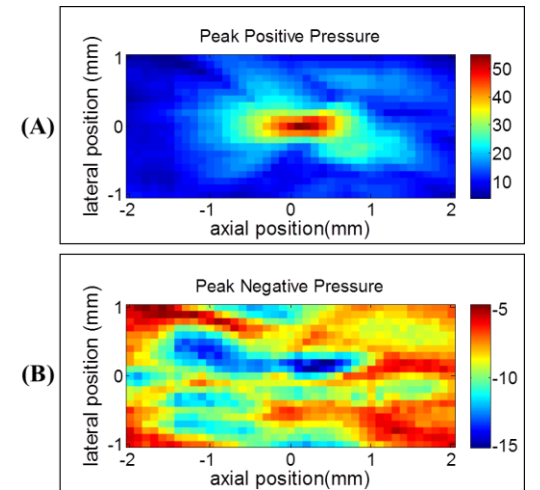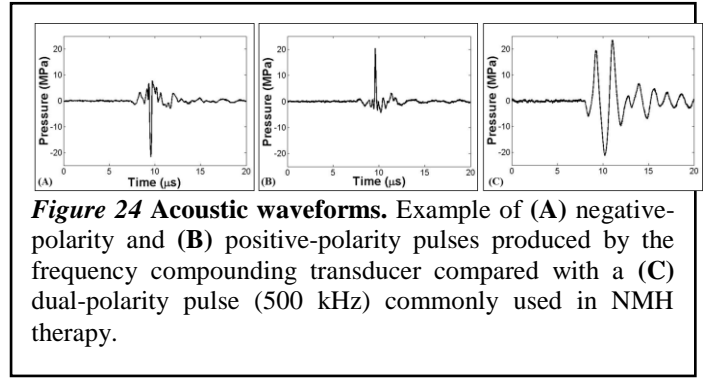
3. *Negative Pressure (P-) Study*

A. Histotripsy Pulse Generation: Histotripsy pulses with dominant negative (negative-polarity pulse) and positive (positive-polarity pulse) pressure phases were generated used a frequency compounding transducer, adapted from a previous study [26]. The frequency-compounding transducer was composed of 12 elements with various resonant frequencies: 500 kHz (three elements), 1 MHz (two elements), 1.5 MHz (two elements), 2 MHz (two elements), and 3 MHz (three elements) [26]. The elements had a common geometric focus at 40 mm

Figure 24 **Acoustic waveforms.** Example of (**A**) negative-polarity and (**B**) positive-polarity pulses produced by the frequency compounding transducer compared with a (**C**) dual-polarity pulse (500 kHz) commonly used in NMH therapy.

and were populated in a scaffold in a specific order to ensure that adjacent elements did not have the same frequency. This was done to reduce nonlinear propagation effects that occur when acoustic waves of the same frequency propagate closely in space and interfere constructively. Additionally, the frequency-compounding transducer has two diametrically opposed optical windows to allow for optical imaging at the geometric focus. The design of the frequency compounding transducer has been described in detail in a previous study [26].

A custom high voltage pulser with 23 parallel channels was used to drive the frequency-compounding transducer. The pulser was connected to a field-programmable gated array (FPGA) development board (Altera DE1, Terasic Technology, Dover, DE, USA) specifically programmed for frequency compounding pulse generation. This setup allowed each element to individually output short pulses with only one large negative or positive pressure phase. The generation of negative-polarity pulses was achieved by adjusting the arrival times of individual frequency components to allow their principal negative phase peaks to arrive at the focus of the transducer concurrently (**Figure 24A**). In this situation, destructive interference occurs elsewhere in space and time, leading to a diminution of the peak positive pressure of the combined ultrasound pulse (**Figure 24A**). For the generation of positive-polarity pulses, the driver pulses for the individual elements were inverted, resulting in ultrasound pulses with a single principal positive phase from each element. The arrival times of individual frequency components were then adjusted to allow their principal positive phase peaks to arrive at the focus concurrently (**Figure 24B**).

A fiber-optic probe hydrophone (FOPH) built in-house [27] was used to calibrate and measure the acoustic output of the frequency-compounding transducer, with example waveforms shown in **Figure 24**. For threshold experiments, the probability of cavitation was plotted as a function of both the peak negative (P–) and peak positive (P+) pressure as measured by the FOPH. In order to determine the peak pressure values for the negative and positive polarity pulses, 2D spatial pressure fields were directly measured using the FOPH in order to identify the locations corresponding to the P– and P+ in the focal region. For the negative-polarity pulses, the P– and P+ occurred at the geometric focus of the transducer. The ratio of P– to P+ measured for the negative-polarity pulses in this location was between 2.9-3.7 for the pressure ranges used in this study. For the positive-polarity pulses, the 2D spatial pressure fields measured by the FOPH

Figure 25 **Positive-polarity Pulse: Pressure Fields.** 2D spatial pressure fields were measured by the FOPH for a positive-polarity pulse. (**A**) Results demonstrated the location corresponding to the highest positive pressure was near the geometric focus. (**B**) The location corresponding to the highest negative pressure was ~0.5 mm away from the geometric focus in the axial direction.

demonstrated the location of the P– in the focal region occurred ~0.5 mm away from the geometric focus, while the location of the P+ remained near the geometric focus (**Figure 25**). This effect is due to the temporal alignment of the principle peak positive peaks of the individual frequency components at the

geometric focus, which resulted in a near monopolar positive pulse at the geometric focus with two low-negative-pressure lobes outside of the focal region. The ratio of P+ to P− for the positive-polarity pulses was measured to be between 3.2-3.9 for the pressure ranges used in this study using the P+ and P− measured at the maximum locations in the field.

B. NMH Cavitation Threshold: Negative-Polarity Pulse:

In the first set of experiments, the histotripsy cavitation threshold was measured for agarose tissue phantoms with and without PFH nanodroplets exposed to negative-polarity pulses (**Figure 24A**). For both types of phantoms, cavitation bubbles were only observed on the high-speed camera once a certain pressure threshold was exceeded (**Figure 26**), as seen in previous studies [15, 22, 28]. As the pressure was further raised

Figure 26 **Bubble Images: Negative-polarity Pulses.** Optical Images of cavitation bubbles generated from negative-polarity pulses inside (**A**) control phantoms and (**B**) PFH phantoms.

above this threshold value, cavitation was observed in an increasingly larger region of the focal area, forming well-defined histotripsy bubble clouds similar to those observed in previous work using dual-polarity pulses at various frequencies [15, 22, 25, 28]. Plotting the probability of cavitation as a function of P− demonstrated a significant decrease in $p_t(-)$ for tissue phantoms containing nanodroplets compared to control phantoms (**Figure 26A,B**), with the P− threshold measured to be $p_{t\_}(-) = 29.8 \pm 0.3$ MPa, with $\sigma_{mean} = 0.7$ MPa for control phantoms without nanodroplets and $p_t(-) = 11.7 \pm 0.2$ MPa, with $\sigma_{mean} = 0.4$ MPa for PFH phantoms. These results closely matched the P− thresholds measured in previous studies using single-cycle dual-polarity pulses with center frequencies ranging from 345kHz to 3MHz. The single-cycle dual-polarity pulses commonly used in histotripsy studies contain both high amplitude positive and negative pressure phases (**Figure 24C**). The P− thresholds for generating cavitation previously measured with the dual-polarity pulse were 24-27 MPa without nanodroplets and 10-15 MPa with PFH nanodroplets[22, 28].

Plotting the probability of cavitation for the negative-polarity pulses as a function of P+ demonstrated a significant decrease in $p_t(+)$ for tissue phantoms containing nanodroplets compared to control phantoms (**Figure 28A,B**), with the P+ threshold measured to be $p_{t\_}(+) = 9.9 \pm 0.1$ MPa, with $\sigma_{mean} = 0.2$ MPa for control phantoms and $p_t(+) = 4.0 \pm 0.1$ MPa, with $\sigma_{mean} = 0.2$ MPa for PFH phantoms. The P+ threshold results measured for the negative-polarity pulses were significantly lower than the P+ thresholds measured in previous studies using dual-polarity pulses, which ranged from $p_t(+) = 28.1$-51.2 MPa and $p_t(+) = 10.2$-15.8 MPa for control and PFH phantoms, respectively.

Figure 27 **Cavitation Probability vs. Negative Pressure.** Plots show the cavitation probability as a function of negative pressure for (**A,C**) control and (**B,D**) PFH phantoms exposed to (**A,B**) negative-polarity pulses and (**C,D**) positive-polarity pulses.

C. NMH Cavitation Threshold: Positive-Polarity Pulse

In the second set of experiments, the histotripsy cavitation threshold was measured for tissue phantoms with and without PFH nanodroplets exposed to positive-polarity pulses (**Figure 24B**). For control phantoms without nanodroplets, cavitation bubbles were not consistently observed in the focal region at any of the pressure levels tested (**Figure 29**). Plotting the probability of cavitation as a function of P− (**Figure 27C**) and P+ (**Figure 28C**) for control phantoms without nanodroplets demonstrated that the cavitation threshold was not reached even when the frequency compounding transducer was driven at its maximum output pressure for the positive-polarity pulses (P−/P+=18.4/61.1 MPa). This finding matched previous work studying the histotripsy intrinsic threshold which has shown that cavitation is only generated when the P− is raised above the intrinsic threshold (~25-30 MPa) [15, 22, 24b, 26].
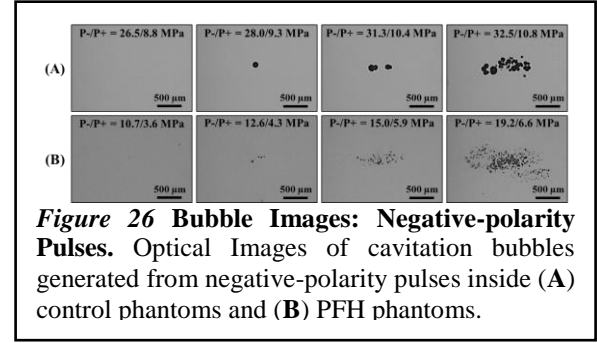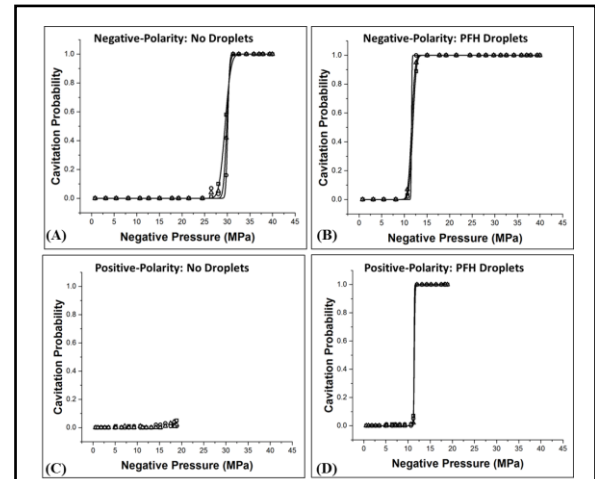
For PFH phantoms exposed to the positive-polarity pulses, cavitation was observed once a certain pressure threshold was exceeded (**Figure 29**). However, cavitation did not occur at the center of the geometric focus of the transducer. Instead, the location of the cavitation was ~0.5 mm from the geometric focus, closely matching the location in the field with the highest P– (**Figure 25**). As the pressure was further increased above the NMH cavitation threshold, two separate regions containing cavitation were observed in the PFH phantoms (**Figure 28**), with these locations closely corresponding to the two regions of highest P– as measured by the FOPH (**Figure 25**). The probability of cavitation for PFH phantoms exposed to positive-polarity pulses was plotted as a function of P– (measured at the location corresponding to the highest P–), with the results demonstrating $p_t(–)$ = 11.4±0.1 MPa, with σ_{mean} = 0.1 MPa (**Figure 27D**). This P– threshold closely matched the P– threshold for the negative-polarity pulses as well as the P– thresholds previously

measured using dual-polarity pulses. Plotting the probability of cavitation for PFH phantoms exposed to positive-polarity pulses as a function of P+ resulted in a P+ threshold of $p_t(+)$ = 42.6±0.2 MPa, with σ_{mean} = 0.4 MPa (**Figure 27D**). This P+ threshold was significantly higher than the P+ thresholds measured for the negative-polarity pulses as well as the P+ thresholds previously measured for dual-polarity pulses. **Figure 30** shows a comparison of the P– and P+ thresholds measured for PFH phantoms exposed to the positive-polarity and negative polarity pulses generated in this study as well as dual-polarity pulses at various frequencies (345 kHz-3MHz) measured in a previous study [28b], with results suggesting that the NMH threshold is a function of the applied P–.

Figure 28 **Cavitation Probability vs. Positive Pressure.** Plots show the cavitation probability as a function of positive pressure for (**A,C**) control and (**B,D**) PFH phantoms exposed to (**A,B**) negative-polarity pulses and (**C,D**) positive-polarity pulses.

Figure 29 **Bubble Images: Positive-polarity Pulses.** Optical Images of cavitation bubbles generated from positive-polarity pulses inside (**A**) control phantoms and (**B**) PFH phantoms. Arrows on the plot indicate the locations in the focal region corresponding to the highest positive (P+) and negative (P–) pressures as measured by the FOPH (**Figure 25**).

In this work, the effects of positive and negative pressure on the NMH cavitation threshold were investigated separately, with results supporting our hypothesis that the NMH cavitation threshold is determined by the incident p-. Close agreement was observed for the P– thresholds measured for PFH tissue phantoms exposed to negative-polarity (11.4±0.1 MPa) and positive-polarity (11.7±0.2 MPa) pulses. The P+ thresholds, in contrast, were significantly different for the negative-polarity (4.0±0.1 MPa) and positive-polarity (42.6±0.2 MPa) pulses. Furthermore, the positive-polarity pulse experiments demonstrated that cavitation was preferentially generated in the regions with the highest P–.

Figure 30 NMH Threshold Results Comparison.

Overall, the results of this study support our hypothesis that nanodroplet nucleation is determined by the applied p- and provide significant insight into the physical mechanisms underlying the NMH process.
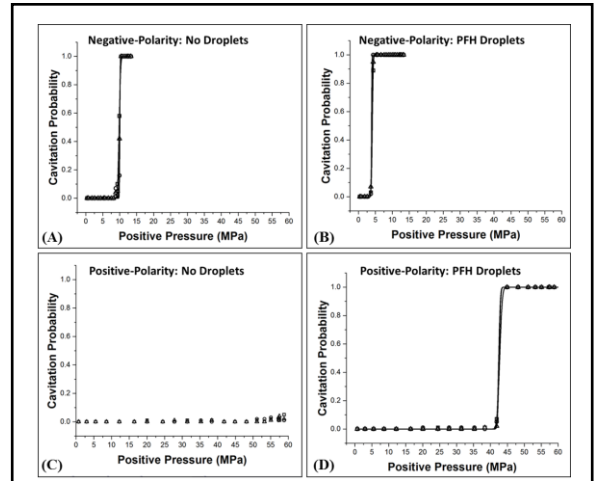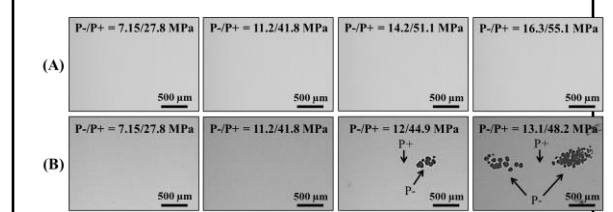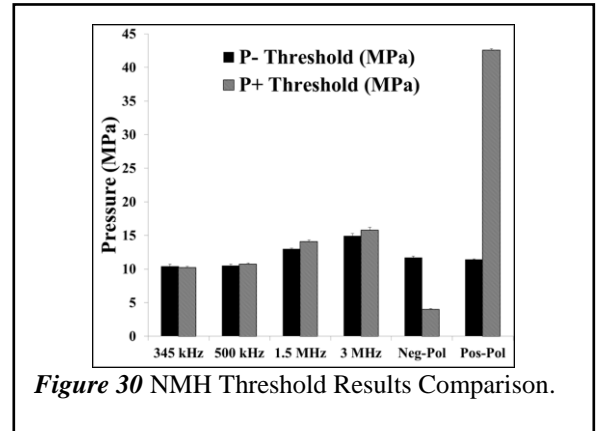
Task 3. Investigate the feasibility of using NMH for precise and efficient multi-foci prostate cancer cell ablation

In task 3, we explored the NMH efficiency on 3D prostate cancer spheroid and planning to do in-vivo experiments based proofed concept in-vitro results. The current results are ready to be published after the in-vivo experiments.

A. PFP or PFH-encapsulation Nanodroplets Characterization: In this study we tested the first time PFP or PFH loaded nanodroplets mediated histotripsy technique efficiency on individual prostate cancer cell lines (C4-2B and PC-3) as well as 3D prostate cancer spheroids that mimic the prostate cancer microenvironment. **Figure 31** demonstrates how to formulate the PFP or PFH-loaded particles self-assembly with triblock fluorinated amphiphilic copolymer composed of a hydrophilic PEG block (A), cross-linkable polyacrylic acid block (PAA) (B), and fluorinated hydrophobic random copolymer of heptadecafluorodecyl methacrylate (HDFMA) and methyl methacrylate (MMA) (C) linked via one-pot "click" reactions. The developed

Figure 31 Schematic presentation showing the formulation of PFP- and PFH-loaded nanodroplets using amphiphilic PEG_{45}-b-$(PAA)_{12}$-b-$P(HDFMA_8$-co-$MMA_{20})$ copolymers.

nanodroplets are ultrasound active particles that can oscillate and burst under ultrasound exposure.

Figure 32 depicts the tumor ablation platform for 3D tumor spheroids. Firstly, the millimeter size spheroids from PC-3 and C4-2B metastatic prostate cancer cell lines were obtained using the ATPS method. The cells were stained with LIVE/DEAD® assay to observe viability of each spheroid. As seen in the Figure 2 (*ii* and *iv*) there are no dead cells (red color), with all cells stained with Calcein AM so they were under green color. Afterward, the formulated PFP/PFH-loaded nanodroplets were incubated with the spheroids. Spheroids were then exposed to the ultrasound pulses to vaporize the nanodroplets delivered to the surface of the tumor nodules, generating a cavitation bubble cloud which mechanically fractionated the cancer cells, leading to destroying the entire tumor.

Figure 32 Schematic drawing of prostate cancer spheroids and images of PC-3 and C4-2B spheroids acquired using light microscope (i and iii) or fluorescence microscope (ii and iv) after staining with Calcein AM dye showing live cancer cells (green). Treatment of prostate cancer spheroids with PFP or PFH-loaded NDs and application of therapeutic ultrasound results in rapid formation and collapse of microbubbles that mechanically fractionate the cancer cells.

In our previous published procedures, we showed that PFP and PFH were able be encapsulated in the fluorinated copolymer forming nanodroplets containing an elastic shell layer within the size of 100-500 nm.[1, 29] These particles were characterized with NTA size analysis system which showed similar characteristics for the PFP and PFH droplets **(Figure 33).** PFP-loaded nanodroplets size spanned between 100 nm to 450 nm with the major peak was less than 300 nm. The average diameter of PFP-loaded nanodroplets was 177 ± 1.9 nm. On the other hand, the size distribution of PFH-loaded nanodroplets was slightly larger than the PFP-loaded ones. The size of PFH-loaded nanodroplets spanned between 100 nm and 600 nm. Moreover, three additional high-intense peaks in the range of 200-300 nm, 300-450 nm, and 450-600 nm

Figure 33 The concentration and size distribution of PFP (blue line) and PFH (red line)-loaded nanodroplets calculated using Nanoparticles Tracking Analysis (NTA).

appeared in the large size portion of the size plot. Because of these additional peaks, the average diameter of the PFH-loaded particles reached to 233.9 ± 3.9 nm. The larger size of the PFH-loaded nanodroplets
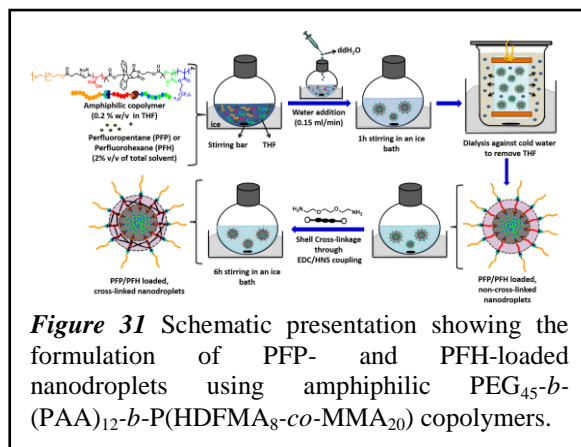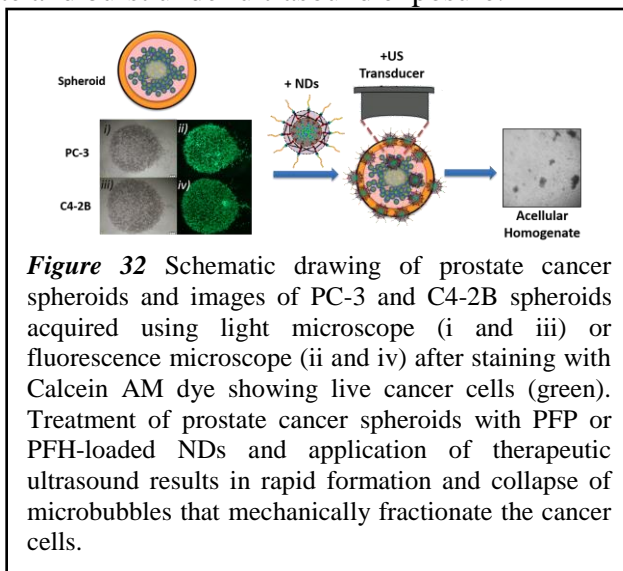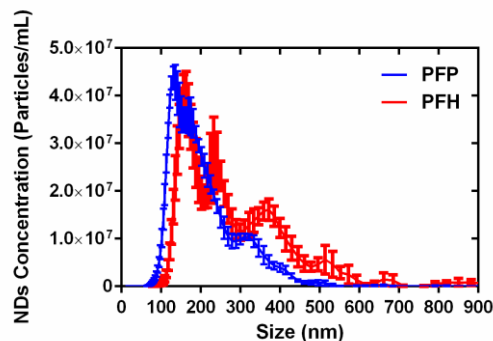
compared to the PFP-loaded nanodroplets might be due to the miscibility character differences between PFP and PFH in the THF/copolymer mixture.

Based on our observation, PFP is able to homogenously dispense in the THF/copolymer mixture in the beginning of particle preparation. However, PFH favors to stay separately from the mixture on the bottom of the round-bottom flask. This energetically tendency phase separation was broken as adding water in drop-wise to trigger the micellization process of the amphiphilic copolymer under vigorous stirring. With this strategy, unmixed PFH in the mixture was made miscible in aqua system via fluorinated-hydrophobic and hydrophilic polymer contents of the amphiphilic copolymer. Both types of droplets were dispersed throughout the medium, and neither droplet type was observed to aggregate together due to the amphiphilic character of the triblock copolymer that stabilized the perfluorocarbons in the core of the nanodroplets as well as enhanced the solubility of the particles with the contribution of hydrophilic PEG corona. Nanodroplet concentration and size characterization demonstrated similar size distributions for the PFP and PFH nanodroplets. The error bars on the size distribution plots represent the standard deviation of the repeat measurements of each sample. The mean size and standard deviation values obtained by the NTA software correspond to arithmetic values calculated with the sizes of all particles analyzed for each sample (n=5). Results from all samples demonstrated an average size of 177.9±1.9 nm and 233.9±3.9 nm for PFP and PFH nanodroplets, respectively. For both types of droplets, >99% of the nanodroplets were smaller than 400 nm and <0.01% were larger than 600 nm. These droplets are in the desired size range, as the desired targeting behavior includes having nanodroplets in the optimal size range for passive targeting through the leaky tumor vasculature (100-400 nm) and reduce the risk of pulmonary embolism[30] by intravenous injection as well as having the functionalized particles for active targeting to tumor cells or other diseased lesions using targeting ligands.

Figure 34 Evaluation of *in vitro* toxicity of PFP- and PFH-loaded nanodroplets towards PC-3 (A) and C4-2B (B) prostate cancer cells as a function of concentration of the polymeric carrier (0-100 μg/mL) with Triton-X 100 positive control.

B. Evaluation of *in vitro* toxicity of PFP- and PFH-loaded nanodroplets:

To investigate the toxicity of the nanodroplet particles, we performed *in vitro* cytotoxicity experiments using a resazurin viability assay. Both prostate cancer cell lines were treated with a variety of concentrations between 0 to 100 mg/mL of PFP or PFH-loaded nanodroplets for 24 h under regular cell culture conditions compared to negative controls of non-treated cells and positive controls of Triton-x 100 treated cells. The results show that both PFC-loaded nanodroplet formulations at any of the tested concentrations have no significant toxic effect on PC-3 (**Figure 34A**) and C4-2B (**Figure 34B**) cells, pointing to biocompatible character of the particles.

C. Ablation of PC-3 and C4-2B individual cells and spheroids in PBS medium:

To investigate the efficiency of nanodroplet-mediated cancer cell ablation, we treated PC-3 and C4-2B cells and spheroids in a home-made rubber tube containing each of our nanodroplet formulation (**Figure 35**) with the controls of no ultrasound and no nanodroplets. Briefly, the cells/spheroids were placed in
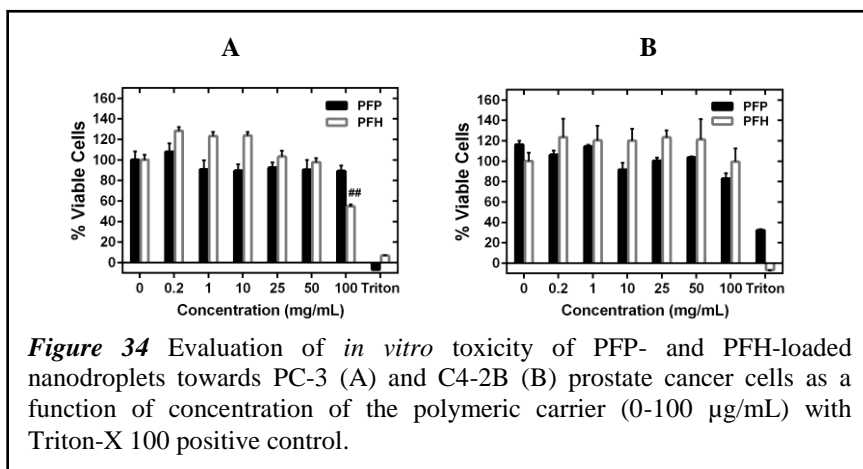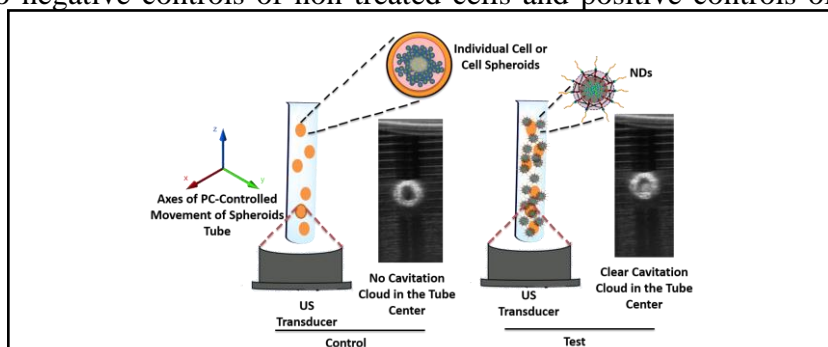

Figure 35 Schematic drawing of the experimental setup incorporating a 345 kHz transducer with the focus aligned to the center of test tubes containing either prostate cancer spheroids alone (control) or spheroids mixed with PFP or PFH-loaded nanodroplets (test). Formation of a bubble cloud in response to histotripsy treatment was monitored using ultrasound imaging. Schematic drawing shows control and test conditions and the expansion of the nanodroplets forming microbubbles (>500μm) in response to histotripsy treatment only in the test group.

the tube within PBS, and the tube was aligned at the focal zone of a twenty-element, 345 kHz array transducer inside a degassed water tank at 37 °C. The 345 kHz ultrasound transducer had a geometric focus of 150 mm, an aperture size of 272 mm, and an effective f-number of 0.55. The tube was positioned with PC-controlled console, and scanned from bottom-to-top and top-to-bottom during 5 min of ultrasound exposure to ensure the focus was exposed to the entire volume within the tube. We hypothesized that ultrasound treatment of the tube with nanodroplets would trigger generate histotripsy cavitation bubbles, causing disruption of the cells around the particles whereas there would not be any bubbles for control samples without nanodroplets under low ultrasound pressure. We tested our hypothesis by applying histotripsy pulses to the center of the cell tube using a pulse repetition frequency of 10 Hz at a peak negative pressure of 10.7 MPa. We inserted an equal number of PFP or PFH-loaded nanodroplets (2×10^8 droplets/mL) in the cell tubes to eliminate the effect of droplets concentration on the observed ablation behavior. In the presence of the nanodroplets in the test conditions, a clear cavitation cloud was generated inside the tubes and observed with real-time on ultrasound imaging using a clinical ultrasound imaging system (HDI 5000 Ultrasound system) (**Figure3 5**). After treatment, the resazurin viability assay was used to assess the cell damage rates formed by histotripsy therapy. Initial results from the control groups (no nanodroplets and no ultrasound, and with nanodroplets no ultrasound) displayed no therapeutic activity for all of the cell lines and spheroids. Further, no nanodroplet but only ultrasound results show that histotripsy application could not initiate significant bubble clouds for both cell lines and spheroids at the applied low acoustic pressure (10.7 MPa) so there was limited killing effect. For example, only ultrasound resulted in

the death of 25% of the PC-3 individual cells and 20% of the C4-2B cell lines **(Figure 36A)**, and around 30% of the PC-3 spheroid cells and 20% of the C4-2B spheroids, which is slightly less therapeutic activity comparing to PC-3 spheroids **(Figure 36B)**. However, upon added nanodroplets to cell/spheroid samples with applied 10.7 MPa ultrasound, we got quite further ablation therapeutic effects. For example, PFP-nanodroplets with ultrasound resulted in the death of almost 80% and 60% of the individual PC-3 and C4-2B cells, respectively (**Figure 36A**).
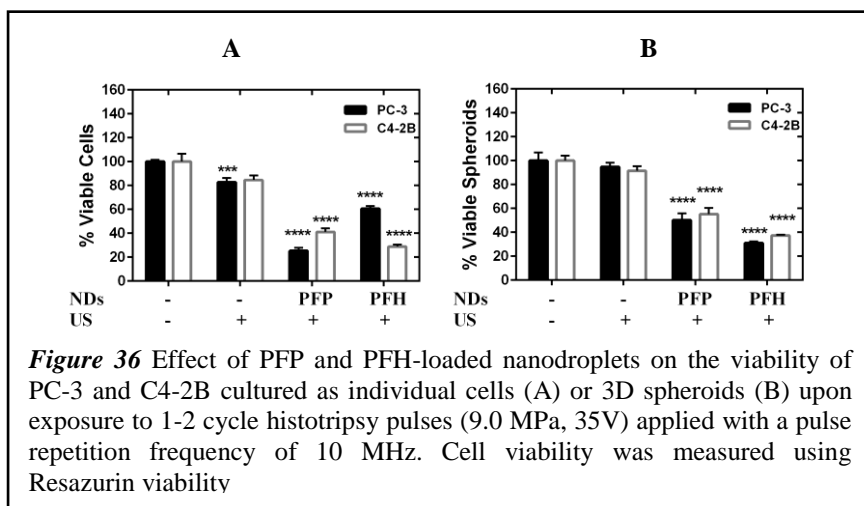

Figure 36 Effect of PFP and PFH-loaded nanodroplets on the viability of PC-3 and C4-2B cultured as individual cells (A) or 3D spheroids (B) upon exposure to 1-2 cycle histotripsy pulses (9.0 MPa, 35V) applied with a pulse repetition frequency of 10 MHz. Cell viability was measured using Resazurin viability
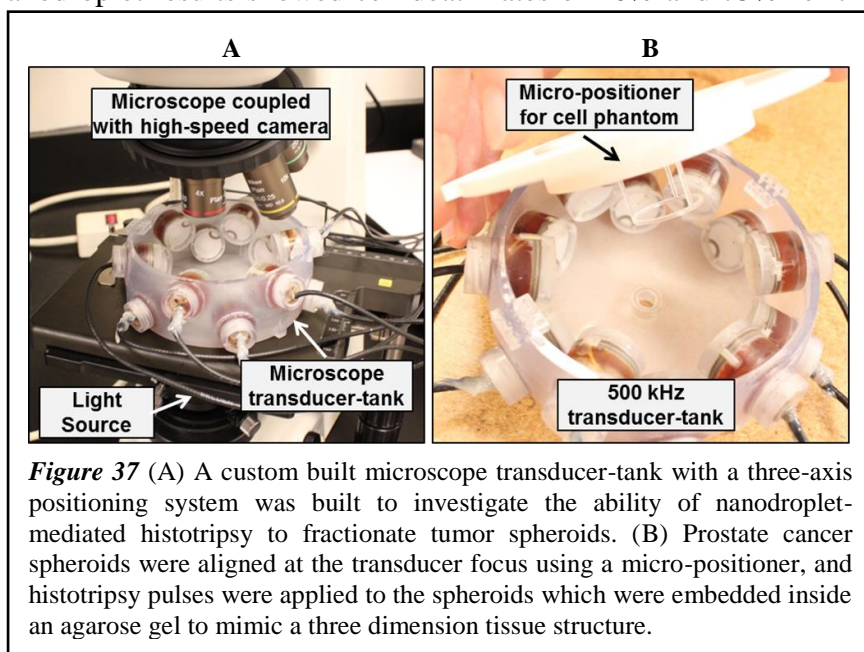
PFH-nanodroplet results showed cell death rates of 40% and 75% for the PC-3 and C4-2B cells, respectively. On the other hand, more than 60% and 50% of the PC-3 and C4-2B spheroids were destroyed with PFP-nanodroplets, respectively. Moreover, the therapeutic activity of PFH-nanodroplets on PC-3 and C4-2B spheroids reached to 70% and 60% cell ablation, respectively **(Figure 36B)**. The nanodroplets containing PFP or PFH resulted in higher cavitation so these offer higher therapeutic activity in response to the histotripsy treatment based on the viability assay results.

D. Nanodroplet-mediated histotripsy on 3D Tumor Model: In

*Figure 37* (A) A custom built microscope transducer-tank with a three-axis positioning system was built to investigate the ability of nanodroplet-mediated histotripsy to fractionate tumor spheroids. (B) Prostate cancer spheroids were aligned at the transducer focus using a micro-positioner, and histotripsy pulses were applied to the spheroids which were embedded inside an agarose gel to mimic a three dimension tissue structure.

the final part of this study, we investigated the cell ablation ability of our nanodroplets on cells and tumor spheroids cultured inside agarose tissue phantoms to better mimic the solid tumor microenvironment. 3D spheroids from PC-3 and C4-2B cell lines were developed using ATPS on agarose tissue phantoms to evaluate the ability of nanodroplet-mediated histotripsy to create tumor fractionation. Previous work exposing histotripsy to agarose tissue phantoms with embedded red blood cell layers have been shown to be similar to ablation generated in tissue identified by histology.[31] To construct the agarose surface, we used degassed 2 % agarose in PBS in which filled of home-made cell-wells. Using this agarose layer allow us to get a tissue mimic phantom and support the millimeter-sized spheroid formation with ATPS. A custom-built miniature transducer tank (**Figure 37**) was designed to generate and image a histotripsy bubble cloud-cell interaction using a microscope coupled with high speed optical imaging (Phantom V210, Vision Research). Agarose gel phantoms with a developed spheroid of prostate cancer cells were used to characterize tissue fractionation induced by nanodroplet-mediated histotripsy. 100 histotripsy pulses were applied to the cell layer with the bubble cloud and the resulting cell fractionation was directly observed and recorded by high-speed optical imaging after each pulse. Nanodroplet-mediated histotripsy resulted in consistent, well-defined fractionation of cancer cells in the region in which cavitation bubbles were observed. The cancer cell fractionation was similar to that seen with histotripsy alone, but at a pressure level well below the histotripsy intrinsic threshold. At the same applied pressure, no cavitation bubbles or cellular damage were observed in the samples without nanodroplets. During the treatments on 3D tumor phantom model such high-pressure and low-pressure with NDs conditions, cavitation bubbles were observed at the transducer focus and cells were observed to be mechanically ruptured. After treatment, no/less cells remained intact in the region in which the histotripsy bubble cloud was observed. At the end of the treatments, the ablated area of the spheroids was calculated with the support of before and after images of ultrafast-recording camera and as well as fluorescence images, which the spheroids were stained with Calcein AM dye to show whether or not the cells were killed. No ND with low-pressure could ablate less than 20% area for both cell lines. However, no ND with high-pressure ablated around 80% of the spheroids. Whereas, with low-pressure, PFP-NDs destroyed 40% of the spheroids, and PFH-NDs could ablate almost 80% of the spheroids **(Figure 38).** These results indicate PFC-loaded NDs significantly reduce the histotripsy threshold, and PFH-loaded NDs with low-pressure can destroy the cells as efficient as high-pressure histotripsy. The increased efficiency observed for PFH droplets might be because of sustainable cavitation nuclei remaining over multiple pulses, as previous work has shown that PFH-loaded nanodroplets can sustain cavitation activity over many pulses, whereas PFP-loaded nanodroplets are destroyed during the initial pulses, likely due to the lower boiling point of the PFP droplets.[29] These results are important to show that nanodroplet-mediated cavitation can indeed create cell disruption and complete fractionation of cancer cells with the same effectiveness as using histotripsy alone but at a significantly lower pressure. This is an important validation of our

Figure 38 Calculation of the fractionated spheroid area after the ablation treatment with low pressure (12.8 MPa), high pressure (26.2 MPa), PFP loaded NDs, or PFH loaded NDs.

hypothesis confirming that the cavitating microbubbles generated via nanodroplets are destructive to use for tumor ablation. If we can perform such treatment to multi-tumor nodules simultaneously with a large focal zone transducer, the treatment efficiency is expected to be greatly improved. Future work will investigate this possibility using a relevant *in vivo* tumor model.
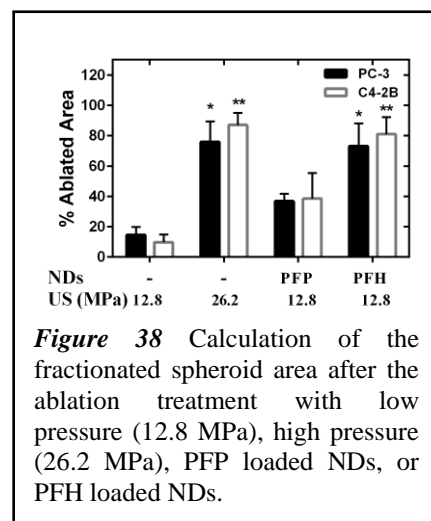
In this study, we showed that NMH could be efficiently used for the ablation of tumors in a relevant 3D microenvironment. These results are a significant advancement upon previous NMH work and suggest that NMH can be used for targeted tumor ablation. Moreover, the significantly reduced pressure threshold using histotripsy combined with NDs should allow for the selective ablation of tumors, while the surrounding normal tissue without NDs would have a higher threshold and be preserved from the histotripsy-induced fractionation. Further, the resulting gas bubbles can function as ultrasound contrast agents, which will allow the tumor sites to be seen on ultrasound imaging and allow the histotripsy treatment to be guided and monitored in real-time by ultrasound imaging. Future work will further investigate these possibilities in order to develop NMH for *in vivo* tumor ablation.

3. KEY RESEARCH ACCOMPLISHMENTS

- A series of amphiphilic block copolymers was synthesized and prescreened to be able to formulate nanodroplets contrast agents with tunable size, PFP content, and shell flexibility to obtain stable and echogenic nanobubbles.

- Self-assembly of most effective two amphiphilic, ABC-1 and ABC-2, polymers around the PFP core with variable PFP content (0%, 1%, and 2% v/v) resulted PFP-loaded nanodroplets in the size range of 100-350 nm.

- Significant decrease in the histotripsy threshold with PFP-loaded nanodroplets (3.10±2,49 MPa) was observed compared to histotripsy alone (15.60±2.35 MPa).

- The similar level of bubble expansion and collapse with histotripsy was observed in agarose gel, the bubble diameter increased to the maximum diameter of 311.2±49.9 μm at 21 μs.

- We were able to ablate Red Blood Cell layer at lower pressure threshold combining nanodroplets with histotripsy.

- Nanodroplets made by ABC-1 with 2% PFP is the most effective composition based on calculated damaged area in the agarose phantom.

- Selective ablation of PFP-Loaded nanodroplets proved that cavitation should be selectively generated in multi-tumor nodules with nanodroplets inside the focal zone, whereas no cavitation should be formed at normal tissue without nanodroplets.

- These nanodroplets have a potential to be used as imaging agent in-vivo

- These nanodroplets maintained their average size and concentration upon incubation with BSA for 24 hours at 37ºC, which prove their promise for cancer cell ablation and warrant their future testing *in vivo*.

- They are not toxic at the level of tested concentration.

- Lower transducer frequency (345 kHz) was shown more effectively worked with NMH comparing to higher frequency (3 MHz).

- PFH-loaded NDs are more stable over 1000 pulses comparing to PFP-loaded NDs.

- Both ND formulations have actively ablated 3D spheroids, however, PFH-NDs with lower pressure (13 MPa) can ablate as much as same efficient with no ND higher pressure (30 MHz).

4. REPORTABLE OUTCOMES

- A manuscript has been published in Molecular Pharmaceutics (Appendix 1)

Yasemin Yuksel Durmaz, Eli Vlaisavljevich, Zhen Xu, Mohamed E.H. ElSayed, and Zhen Xu, "Development of nanodroplets for histotripsy-mediated cell ablation", *Molecular Pharmaceutics*, 11(10): 3684-3695, 2014.

- A manuscript has been published in Theranostic (Appendix 2)

Eli Vlaisavljevich, Yasemin Yuksel Durmaz, Adam Maxwell, Mohamed E.H. ElSayed, and Zhen Xu, "Nanodroplet-mediated histotripsy for image-guided targeted ultrasound cell ablation", *Theranostics*, 3(11): 851-864, 2013.

- A manuscript has been published in Ultrasound in Medicine and Biology (Appendix 3)

Eli Vlaisavljevich, Omer Aydin, Yasemin Yuksel Durmaz, Kuang-Wei Lin, Brain Fowlkes, Mohamed E.H. ElSayed, and Zhen Xu, "The Effects of Ultrasound Frequency on Nanodroplet-Mediated Histotripsy'", *Ultrasound in Medicine and Biology*, 41(8), 2135, 2015.

- Another one is under review (Appendix 4)

E. Vlaisavljevich, O. Aydin, Y. Y. Durmaz, K-W Lin, B. Fowlkes, Z. Xu, and M. ElSayed "The Effects of Droplet Composition on Nanodroplet-Mediated Histotripsy".

- Another one is under review (Appendix 5)

E. Vlaisavljevich, O. Aydin, Y. Y. Durmaz, K-W Lin, B. Fowlkes, M. ElSayed, and Z. Xu "The Role of Positive and Negative Pressure on Cavitation Nucleation in Nanodroplet-Mediated Histotripsy".

- Manuscript in preparation (Appendix 6)

O. Aydin, E. Vlaisavljevich, Y. Y. Durmaz, M. ElSayed, Z. Xu, "Nanodroplet-Mediated Histotripsy of 3D Metastatic Prostate Cancer Spheroid Ablation".

CONFERENCE PROCEEDINGS

- O. Aydin, E. Vlaisavljevich Y. Y. Durmaz, Z. Xu, and M. E. H. ElSayed, "Nanodroplet Mediated Histotripsy Validation on 3D Prostate Cancer Models", EGS, October, 2015, Ann Arbor, Michigan.

- O. Aydin, E. Vlaisavljevich Y. Y. Durmaz, Z. Xu, M. E. H. ElSayed, "Nanodroplet Mediated Histotripsy (NMH) Cell Ablation on 3D Prostate Cancer Models", 39th Macromolecular Symposium, October, 2015, Ann Arbor, Michigan.

- O. Aydin, E. Vlaisavljevich Y. Y. Durmaz, Z. Xu, and M. E. H. ElSayed, "A Nanomedicine Solution for Focal Prostate Cancer Treatment: Nanodroplet Mediated Histotripsy (NMH)", BMES Annual Meeting, October, 2015, Tampa, Florida.

- O. Aydin, E. Vlaisavljevich Y. Y. Durmaz, Z. Xu, M. E. H. ElSayed, "Nanodroplet Mediated Histotripsy (NMH) Cell Ablation on 3D Prostate Cancer Models", 13th International Nanomedicine & Drug Delivery Symposium, NanoDDS15, September 2015, Seattle, Washington.

- E. Vlaisavljevich, O. Aydin, K.-W. Lin, B. Fowlkes, M. E.H. ElSayed, and Zhen Xu, "Investigation of the role of ultrasound frequency and droplet composition in nanodroplet-mediated histotripsy", International Society for Therapeutic Ultrasound, April, 2015, Utrecht, Netherlands.

5. CONCLUSION

To summarize, in the beginning we designed and synthesized several amphiphilic PEG_x-*b*-$(PAA)_y$-*b*-$P(HDFMA_z$-*co*-$MMA_w)$ copolymers that proved to encapsulate 1%-2% v/v PFP forming nanodroplets. Combining histotripsy pulses with nanodroplets formulated using these copolymers proved to generate a cavitation bubble cloud that ablates neighboring RBCs at reduced acoustic pressure compared to histotripsy alone. In next studies we investigated to understand the fundamental of the nanodroplet mediated histotripsy by changing frequency, the core PFC component of the NDs, and peak negative pressure (P-). Results demonstrated that the NMH threshold was significantly reduced at lower frequency, ranging from 7.4 MPa at 345 kHz to 13.2 MPa at 3 MHz. Furthermore, results demonstrated that NMH bubble expansion was enhanced at lower frequency, generating bubbles with a maximum radius >100 µm despite the reduced pressure applied. The effects of droplet composition on NMH therapy were investigated using perfluoropentane (boiling point~29°C, surface tension~9.5 mN/m) and perfluorohexane (boiling point~56°, surface tension~1.2 mN/m) droplets. The results demonstrated a significant decrease in the cavitation threshold for both types of nanodroplets compared to controls, with a slightly lower threshold observed for PFP phantoms, likely due to the decrease in surface tension for PFP. Results further demonstrated that PFH nanodroplets were sustainable cavitation nuclei over multiple pulses, while PFP nanodroplets were destroyed during the initial pulses. This effect is most likely due to the re-condensing of PFH droplets into a liquid after the cavitation event occurs, due to the higher boiling point of the PFH droplets. Moreover, we found that the NMH cavitation threshold is determined by the incident *p*-. Lastly, we showed that NMH could be efficiently used for the ablation of tumors in a relevant 3D microenvironment. These results are a significant advancement upon previous NMH work and suggest that NMH can be used for targeted tumor ablation. Moreover, the significantly reduced pressure threshold using histotripsy combined with NDs should allow for the selective ablation of tumors, while the surrounding normal tissue without NDs would have a higher threshold and be preserved from the histotripsy-induced fractionation. Further, the resulting gas bubbles can function as ultrasound contrast agents, which will allow the tumor sites to be seen on ultrasound imaging and allow the histotripsy treatment to be guided and monitored in real-time by ultrasound imaging. Future work will further investigate these possibilities in order to develop NMH for *in vivo* tumor ablation.

6. References

1.   Yuksel Durmaz, Y.; Vlaisavljevich, E.; Xu, Z.; ElSayed, M., Development of nanodroplets for histotripsy-mediated cell ablation. *Mol Pharm* **2014,** *11* (10), 3684-95.

2.   (a) Mendizabal, M.; Reddy, K. R., Current management of hepatocellular carcinoma. *Med Clin North Am* **2009,** *93* (4), 885-900; (b) Kudo, M., Radiofrequency ablation for hepatocellular carcinoma: updated review in 2010. *Oncology.* **2010,** *78* (Suppl 1), 113-24. Epub 2010 Jul 8.

3.   (a) Gazelle, G. S.; Goldberg, S. N.; Solbiati, L.; Livraghi, T., Tumor ablation with radio-frequency energy. *Radiology.* **2000,** *217* (3), 633-46; (b) Illing, R. O.; Kennedy, J. E.; Wu, F.; ter Haar, G. R.; Protheroe, A. S.; Friend, P. J.; Gleeson, F. V.; Cranston, D. W.; Phillips, R. R.; Middleton, M. R., - The safety and feasibility of extracorporeal high-intensity focused ultrasound (HIFU) for the treatment of liver and kidney tumours in a Western population. *Br J Cancer* **2005,** *93* (8), 890-5.

4.   (a) Sheeran, P. S.; Wong, V. P.; Luois, S.; McFarland, R. J.; Ross, W. D.; Feingold, S.; Matsunaga, T. O.; Dayton, P. A., Decafluorobutane as a Phase-Change Contrast Agent for Low-Energy Extravascular Ultrasonic Imaging. *Ultrasound in Medicine and Biology* **2011,** *37* (9), 1518-1530; (b) Wilson, K.; Homan, K.; Emelianov, S., Biomedical photoacoustics beyond thermal expansion using triggered nanodroplet vaporization for contrast-enhanced imaging. *Nature communications* **2012,** *3*, 618 (10 pp.); (c) Rapoport, N.; Nam, K. H.; Gupta, R.; Gao, Z.; Mohan, P.; Payne, A.; Todd, N.; Liu, X.; Kim, T.; Shea, J.; Scaife, C.; Parker, D. L.; Jeong, E. K.; Kennedy, A. M., Ultrasound-mediated tumor imaging and nanotherapy using drug loaded, block copolymer stabilized perfluorocarbon nanoemulsions. *J Control Release* **2011,** *153* (1), 4-15; (d) Kawabata, K. i.; Asami, R.; Azuma, T.; Umemura, S. i., Acoustic Response of Microbubbles Derived from Phase-change Nanodroplet. *Japanese Journal of Applied Physics* **2010,** *49* (7), 07HF18 (9 pp.).

5.   (a) Rapoport, N. Y.; Nam, K. H.; Gao, Z.; Kennedy, A., Application of ultrasound for targeted nanotherapy of malignant tumors. *Acoustical Physics* **2009,** *55* (4-5), 594-601; (b) Rapoport, N.; Nam, K.-H.; Gupta, R.; Gao, Z.; Mohan, P.; Payne, A.; Todd, N.; Liu, X.; Kim, T.; Shea, J.; Scaife, C.; Parker, D. L.; Jeong, E.-K.; Kennedy, A. M. In *Ultrasound-mediated tumor imaging and nanotherapy using drug loaded, block copolymer stabilized perfluorocarbon nanoemulsions*, P.O. Box 211, Amsterdam, 1000 AE, Netherlands, Elsevier: P.O. Box 211, Amsterdam, 1000 AE, Netherlands, 2011; pp 4-15.

6.   (a) Kieran, K.; Hall, T. L.; Parsons, J. E.; Wolf, J. S., Jr.; Fowlkes, J. B.; Cain, C. A.; Roberts, W. W., Refining histotripsy: defining the parameter space for the creation of nonthermal lesions with high intensity, pulsed focused ultrasound of the in vitro kidney. *J Urol* **2007,** *178* (2), 672-6; (b) Winterroth, F.; Xu, Z.; Wang, T. Y.; Wilkinson, J. E.; Fowlkes, J. B.; Roberts, W. W.; Cain, C. A., Examining and analyzing subcellular morphology of renal tissue treated by histotripsy. *Ultrasound Med Biol* **2011,** *37* (1), 78-86; (c) Xu, Z.; Fan, Z.; Hall, T. L.; Winterroth, F.; Fowlkes, J. B.; Cain, C. A., Size measurement of tissue debris particles generated from pulsed ultrasound cavitational therapy-histotripsy. *Ultrasound Med Biol* **2009,** *35* (2), 245-55; (d) Xu, Z.; Fowlkes, J. B.; Cain, C. A., A new strategy to enhance cavitational tissue erosion using a high-intensity, Initiating sequence. *IEEE Trans Ultrason Ferroelectr Freq Control* **2006,** *53* (8), 1412-24; (e) Xu, Z.; Fowlkes, J. B.; Rothman, E. D.; Levin, A. M.; Cain, C. A., Controlled ultrasound tissue erosion: the role of dynamic interaction between insonation and microbubble activity. *J Acoust Soc Am* **2005,** *117* (1), 424-35.

7.   (a) Gao, Z.; Kennedy, A. M.; Christensen, D. A.; Rapoport, N. Y., Drug-loaded nano/microbubbles for combining ultrasonography and targeted chemotherapy. *Ultrasonics.* **2008,** *48* (4), 260-70. Epub 2007 Nov 19; (b) Kawabata, K. i.; Asami, R.; Yoshikawa, H.; Azuma, T.; Umemura, S. i., Sustaining Microbubbles Derived from Phase Change Nanodroplet by Low-Amplitude Ultrasound Exposure. *Japanese Journal of Applied Physics* **2010,** *49* (7), 07HF20 (4 pp.); (c) Sheeran, P. S.; Luois, S.; Dayton, P. A.; Matsunaga, T. O., Formulation and acoustic studies of a new phase-shift agent for diagnostic and therapeutic ultrasound. *Langmuir* **2011,** *27* (17), 10412-20.

8.   Perrier, S.; Jackson, S. G.; Haddleton, D. M.; Ameduri, B.; Boutevin, B., Preparation of fluorinated methacrylic copolymers by copper mediated living radical polymerization. *Tetrahedron* **2002,** *58* (20), 4053-4059.

9.   (a) Sun, X. K.; Rossin, R.; Turner, J. L.; Becker, M. L.; Joralemon, M. J.; Welch, M. J.; Wooley, K. L., An assessment of the effects of shell cross-linked nanoparticle size, core composition, and surface PEGylation on in vivo biodistribution. *Biomacromolecules* **2005,** *6* (5), 2541-2554; (b) Nam, K.; Kimura, T.; Kishida, A., Controlling coupling reaction of EDC and NHS for preparation of collagen gels using ethanol/water co-solvents. *Macromolecular Bioscience* **2008,** *8* (1), 32-37.

10.   Deschamps, A. A.; Grijpma, D. W.; Feijen, J., Poly(ethylene oxide)/poly(butylene terephthalate) segmented block copolymers: the effect of copolymer composition on physical properties and degradation behavior. *Polymer* **2001,** *42* (23), 9335-9345.

11.   (a) Gao, Z.; Kennedy, A. M.; Christensen, D. A.; Rapoport, N. Y., Drug-loaded nano/microbubbles for combining ultrasonography and targeted chemotherapy. *Ultrasonics* **2008,** *48* (4), 260-270; (b) Sheeran, P. S.; Luois, S.; Dayton, P. A.; Matsunaga, T. O., Formulation and Acoustic Studies of a New Phase-Shift Agent for Diagnostic and Therapeutic Ultrasound. *Langmuir* **2011,** *27* (17), 10412-10420.

12.   Maxwell, A. D.; Wang, T. Y.; Yuan, L. Q.; Duryea, A. P.; Xu, Z.; Cain, C. A., A Tissue Phantom for Visualization and Measurement of Ultrasound-Induced Cavitation Damage. *Ultrasound in Medicine and Biology* **2010,** *36* (12), 2132-2143.

13.   (a) Shiraishi, K.; Endoh, R.; Furuhata, H.; Nishihara, M.; Suzuki, R.; Maruyama, K.; Oda, Y.; Jo, J.; Tabata, Y.; Yamamoto, J.; Yokoyama, M., A facile preparation method of a PFC-containing nano-sized emulsion for theranostics of solid tumors. *International Journal of Pharmaceutics* **2011,** *421* (2), 379-387; (b) Nishihara, M.; Imai, K.; Yokoyama, M., Preparation of Perfluorocarbon/Fluoroalkyl Polymer Nanodroplets for Cancer-targeted Ultrasound Contrast Agents. *Chemistry Letters* **2009,** *38* (6), 556-557.

14.   Leighton, T. G., *The Acoustic Bubble*. Academic Press 1994.

15.   Maxwell, A. D.; Cain, C. A.; Hall, T. L.; Fowlkes, J. B.; Xu, Z., Probability of cavitation for single ultrasound pulses applied to tissues and tissue-mimicking materials. *Ultrasound Med Biol* **2013,** *39* (3), 449-65.

16.   Hosmer, D. W.; Lemeshow, S., Confidence interval estimation of interaction. *Epidemiology* **1992,** *3* (5), 452-6.

17.	Vlaisavljevich, E.; Warnez, M.; Johnsen, E.; Singh, R.; Putnam, A.; Xu, Z., Investigation of the role of tissue stiffness and ultrasound frequency in histotripsy-induced cavitation. . *Symposium on Therapeutic Ultrasound* **2014**.

18.	Vlaisavljevich, E.; Durmaz, Y. Y.; Maxwell, A.; Elsayed, M.; Xu, Z., Nanodroplet-mediated histotripsy for image-guided targeted ultrasound cell ablation. *Theranostics* **2013,** *3* (11), 851-64.

19.	(a) Dobrovolskaia, M. A.; Aggarwal, P.; Hall, J. B.; McNeil, S. E., Preclinical studies to understand nanoparticle interaction with the immune system and its potential effects on nanoparticle biodistribution. *Mol Pharm* **2008,** *5* (4), 487-95; (b) Kim, D.; El-Shall, H.; Dennis, D.; Morey, T., Interaction of PLGA nanoparticles with human blood constituents. *Colloids Surf B Biointerfaces* **2005,** *40* (2), 83-91.

20.	Torchilin, V., Tumor delivery of macromolecular drugs based on the EPR effect. *Adv Drug Deliv Rev* **2011,** *63* (3), 131-5.

21.	Kusnetzky, L. L.; Khalid, A.; Khumri, T. M.; Moe, T. G.; Jones, P. G.; Main, M. L., Acute mortality in hospitalized patients undergoing echocardiography with and without an ultrasound contrast agent: results in 18,671 consecutive studies. *J Am Coll Cardiol* **2008,** *51* (17), 1704-6.

22.	Vlaisavljevich, E.; Lin, K. W.; Maxwell, A.; Warnez, M.; Mancia, L.; Singh, R.; Putnam, A.; Fowlkes, J. B.; Johnsen, E.; Cain, C.; Xu, Z., Effects of Ultrasound Frequency and Tissue Stiffness on the Histotripsy Intrinsic Threshold for Cavitation. *Ultrasound Med Biol* **2015**.

23.	Fabiilli, M. L.; Wilson, C. G.; Padilla, F.; Martin-Saavedra, F. M.; Fowlkes, J. B.; Franceschi, R. T., Acoustic droplet-hydrogel composites for spatial and temporal control of growth factor delivery and scaffold stiffness. *Acta Biomater* **2013,** *9* (7), 7399-409.

24.	(a) Wang, T. Y.; Xu, Z.; Hall, T. L.; Fowlkes, J. B.; Cain, C. A., An efficient treatment strategy for histotripsy by removing cavitation memory. *Ultrasound Med Biol* **2012,** *38* (5), 753-66; (b) Lin, K. W.; Kim, Y.; Maxwell, A. D.; Wang, T. Y.; Hall, T. L.; Xu, Z.; Fowlkes, J. B.; Cain, C. A., Histotripsy beyond the intrinsic cavitation threshold using very short ultrasound pulses: microtripsy. *IEEE Trans Ultrason Ferroelectr Freq Control* **2014,** *61* (2), 251-65.

25.	Vlaisavljevich, E.; Lin, K. W.; Warnez, M.; Singh, R.; Mancia, L.; Putnam, A.; Johnsen, E.; Cain, C.; Xu, Z., Effects of Tissue Stiffness, Ultrasound Frequency, and Pressure on Histotripsy-induced Cavitation Bubble Behavior. *Phys Med Biol* **2015**.

26.	Lin, K. W.; Hall, T. L.; McGough, R. J.; Xu, Z.; Cain, C. A., Synthesis of monopolar ultrasound pulses for therapy: the frequency-compounding transducer. *IEEE Trans Ultrason Ferroelectr Freq Control* **2014,** *61* (7), 1123-36.

27.	Parsons, J. E.; Cain, C. A.; Fowlkes, J. B., Cost-effective assembly of a basic fiber-optic hydrophone for measurement of high-amplitude therapeutic ultrasound fields. *J Acoust Soc Am* **2006,** *119* (3), 1432-40.

28.	(a) Vlaisavljevich, E.; Aydin, O.; Durmaz, Y. Y.; Lin, K. W.; Fowlkes, J. B.; ElSayed, M.; Xu, Z., The Effects of Ultrasound Frequency on Nanodroplet-Mediated Histotripsy. *Ultrasound Med Biol* **2015**; (b) Vlaisavljevich, E.; Aydin, O.; Lin, K. W.; Fowlkes, J. B.; ElSayed, M.; Xu, Z., Investigation of the Role of Ultrasound Frequency and Droplet Composition in Nanodroplet-mediated Histotripsy. In *International Society for Therapeutic Ultrasound*, Utrecht, Netherlands, 2015.

29.	Vlaisavljevich, E.; Aydin, O.; Lin, K. W.; Fowlkes, B.; El-Sayed, M.; Xu, Z., Investigation of the role of ultrasound frequency and droplet composition in nanodroplet-mediated histotripsy. In *International Society for Therapeutic Ultrasound*, Utrecht, Netherlands, 2015.

30.	Butler, B. D.; Hills, B. A., The lung as a filter for microbubbles. *J Appl Physiol Respir Environ Exerc Physiol* **1979,** *47* (3), 537-43.

31.	Maxwell, A. D.; Wang, T. Y.; Yuan, L.; Duryea, A. P.; Xu, Z.; Cain, C. A., A tissue phantom for visualization and measurement of ultrasound-induced cavitation damage. *Ultrasound Med Biol* **2010,** *36* (12), 2132-43.

7. APPENDICES:N/A

8.   SUPPORTING DATA: N/A